

See discussions, stats, and author profiles for this publication at: <https://www.researchgate.net/publication/224224811>

Identification of a Bipedal Robot with a Compliant Drivetrain

Article in IEEE control systems · May 2011

DOI: 10.1109/MCS.2010.939963 · Source: IEEE Xplore

CITATIONS

64

READS

1,549

4 authors, including:



Hae-Won Park

Massachusetts Institute of Technology

11 PUBLICATIONS 892 CITATIONS

[SEE PROFILE](#)



Jonathan W. Hurst

Oregon State University

51 PUBLICATIONS 2,129 CITATIONS

[SEE PROFILE](#)

Some of the authors of this publication are also working on these related projects:



Project Bipedal Robotic Locomotion [View project](#)

Identification of a Bipedal Robot with a Compliant Drivetrain

PARAMETER ESTIMATION FOR CONTROL DESIGN



HAE-WON PARK,
KOUSHIL SREENATH,
JONATHAN W. HURST,
and JESSY W. GRIZZLE

Research in bipedal robotics aims to design machines with the speed, stability, agility, and energetic efficiency of a human. While no machine built today realizes the union of these attributes, several robots demonstrate one or more of them. The Cornell biped is designed to be highly energy efficient [1]. This robot walks with a dimensionless mechanical-transport cost c_{mt} of 0.055; the corresponding efficiency for a typical human is 0.05. The down side of this achievement is that the robot can walk on only flat ground; it trips and falls in the presence of ground variations of a few millimeters. The Planar biped, which excels at agility, can run stably on one or two legs, hop up and down stairs, and can bound over piles of blocks, but does not walk well [2]–[4]. This robot is inefficient due to its pneumatic and hydraulic actuation. Moreover, the physical principles that underlie its mechanical design and control system are difficult to generalize to other machines. The bipedal robot Rabbit exhibits

PHOTO BY HAE-WON PARK AND KOUSHIL SREENATH

Digital Object Identifier 10.1109/MCS.2010.939963
Date of publication: 16 March 2011

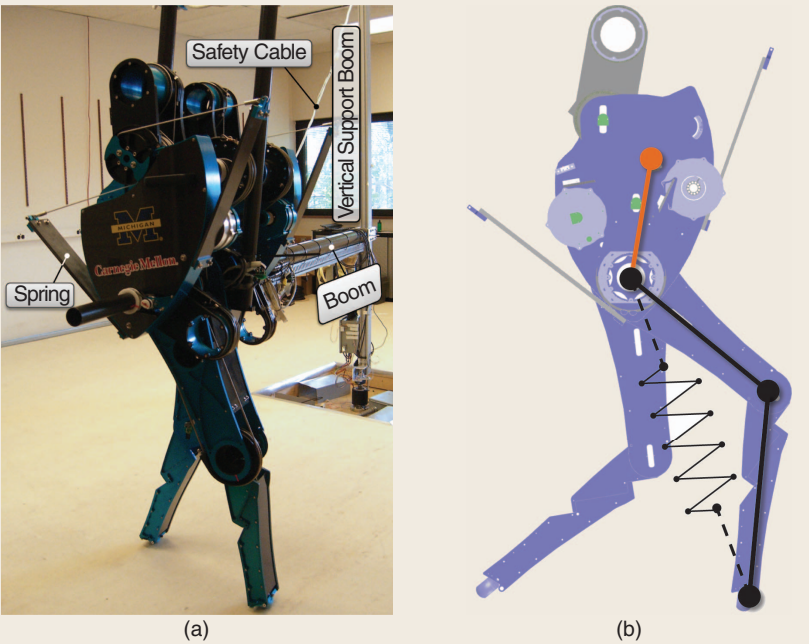


FIGURE 1 MABEL, a planar bipedal robot for walking and running. (a) The shin and thigh are each 50 cm long, making the robot 1 m tall at the hip. The overall mass is 60 kg, excluding the boom. The boom provides side-to-side stability because the hips are revolute joints allowing only forward and backward motion of the legs. The safety cable prevents the knees and torso from hitting the lab floor when the robot falls. (b) The robot incorporates springs for shock absorption and energy storage. Differentials housed in the robot's torso create a virtual prismatic leg with compliance.

robustly stable walking under model-based control [5], [6]; a controller implemented on the robot in 2002 still functions today. On the other hand, Rabbit can run only a few steps without falling [7], and its mechanical-transport cost is 0.38.

MABEL, shown in Figure 1, aims to achieve a better overall compromise in speed, stability, agility, and energy efficiency. This robot can be thought of as a hybrid of the Planar biped and Rabbit. MABEL's drivetrain uses motors, cable differentials, and springs to create a virtual, series-compliant leg between the hip and the toe [8]. This series-compliance absorbs shocks when the legs impact the ground, increasing stability robustness through disturbance attenuation, and also stores energy, thereby improving efficiency. MABEL walks at 1.5 m/s, which was the record bipedal-walking-robot speed from April 2010 through October 2010 [9].

The feedback control and gait design in [9] are based on a simplified model of MABEL. Data reported in [9] show significant discrepancies between this model and experiment. For example, the compliance in the robot is inadequately modeled, with predicted and measured spring deflections differing at times by 30% during a walking gait. In addition, the simplified model predicts a dimensionless mechanical-transport cost c_{mt} of 0.04, while it is experimentally measured to be 0.15.

The primary objective of this article is to identify the parameters that appear in a dynamic model of MABEL. This model is appropriate for the design and analysis of feedback controllers for bipedal locomotion. The parameters we seek to identify include inertias, center-of-mass locations, spring constants, motor torque constants, friction coefficients, and power-amplifier biases. We plan to use the identified model to further improve the speed, stability, agility, and energetic efficiency of MABEL.

The problem of parameter identification for robot models is well studied in the literature [10]–[13]. Most results are based on the analysis of the input-output behavior of the robot during a planned motion, where the parameter values are obtained by minimizing the difference between a function of the measured robot variables and the output of the model. An illustration of this approach is presented in [11] for identifying parameters in industrial manipulators. The standard rigid-body model is rewritten in the parametric form $\tau = \phi(q, \dot{q}, \ddot{q})\theta$, which is linear in the unknown parameters,

where q , \dot{q} , \ddot{q} are the position, velocities, and accelerations of the joints; τ is the vector of joint torques; θ is the unknown parameter vector; and ϕ is the regressor matrix. Optimization is used to define trajectories that enhance the condition number of ϕ , and these trajectories are then executed on the robot. Weighted least-squares estimation is applied to estimate the parameters, which in turn are validated by torque prediction. This approach requires acceleration, which must be estimated numerically from measured position.

An alternative approach explored in [12] uses force- and torque-sensor measurements to avoid the need to estimate acceleration. The robot model is represented in Newton-Euler form, and a six-element wrench at the robot's wrist is expressed in a form that is linear in the unknown parameters. Force and torque at the wrist are measured directly through force and torque sensors, and parameter estimation is accomplished from this data without the need for acceleration measurements. Another class of methods [13] uses an energy-based model that uses velocity and position variables but does not require acceleration. This method, however, relies on the integration of the input torques and the joint velocities to compute energy, which is problematic if the torque estimates are corrupted by an unknown bias.

MABEL aims to achieve a better overall compromise in speed, stability, agility, and energy efficiency.

Parameter identification for MABEL is a challenging task for several reasons. First, MABEL has position encoders at the motors and joints, as well as contact switches at the leg ends, but lacks force and torque sensors. We thus use commanded motor torques as inputs and motor and joint position encoders as outputs to extract model parameters. Due to the quantization error of the encoders, it is difficult to estimate acceleration by numerically differentiating encoder signals. Hence, we estimate parameters without calculating acceleration from position data. Second, the actuator characteristics are poorly known. The motors used in MABEL are brushless direct current (BLDC) motors, which are custom manufactured on demand. Due to the small production numbers, the rotor inertias and torque constants may differ by 20% from the values supplied by the manufacturer. These parameters must therefore be included in the identification procedure. In combination with power amplifiers from a second manufacturer, the motors exhibit some directional bias. Complicating matters further, this bias varies among individual amplifier-motor pairs. Consequently, the amplifier bias must be considered in the identification process. A third issue affecting parameter identification is that the choice of exciting trajectory is restricted due to limitations of MABEL's work space. For example, a constant-velocity experiment for estimating friction coefficients is not feasible because the maximum range of rotation of each joint is less than 180°. Finally, because MABEL has many degrees of freedom, actuating all of them at once would require estimating 62 parameters simultaneously. For this reason, we take advantage of the modular nature of the robot to design experiments that allow us to sequentially build the model element by element, estimating only a few parameters at each stage of the process.

MECHANISM OVERVIEW

MABEL's body consists of five links, namely, a torso, two thighs, and two shins. The hip of the robot is attached to a boom, as shown in Figure 2. The robot's motion is therefore tangent to a sphere centered at the pivot point of the boom on the central tower. The boom is 2.25 m long, and while the resulting walking motion of the robot is circular, it approximates the motion of a planar biped walking along a straight line.

The actuated degrees of freedom of each leg do not correspond to the knee and the hip angles as in a conventional biped. Instead, as shown in figures 3 and 4, for each leg, a collection of differentials is used to connect two motors to the hip and knee joints in such a way that one motor controls

the angle of the virtual leg defined by the line connecting the hip to the toe, while the second motor is connected in series with a spring to control the length of the virtual leg. Conventional bipedal robot coordinates and MABEL's actuated coordinates, which are depicted in Figure 4, are related by

$$q_{LA} = \frac{1}{2}(q_{Th} + q_{Sh}) \quad (1)$$

and

$$q_{LS} = \frac{1}{2}(q_{Th} - q_{Sh}), \quad (2)$$

where LA stands for leg angle, LS stands for leg shape, Th stands for thigh, and Sh stands for shin.

The springs in MABEL isolate the leg-shape motors from the impact forces at leg touchdown. In addition, the springs store energy during the compression phase of a running gait, when the support leg must decelerate the downward motion of the robot's center of mass. The energy stored in the spring can then be used to redirect the center of mass upwards for the subsequent flight phase, propelling the robot off the ground. As explained in [14]–[16], both of these properties, shock isolation and energy storage, enhance the energy efficiency of running and reduce the actuator power requirements. Similar advantages are also present in walking on flat ground, but to a lesser extent compared to running on uneven terrain, due to the lower forces at leg impact and the reduced vertical travel of the center of mass. The robotics literature strongly suggests that shock isolation and compliance are useful for walking on uneven terrain [17]–[23].

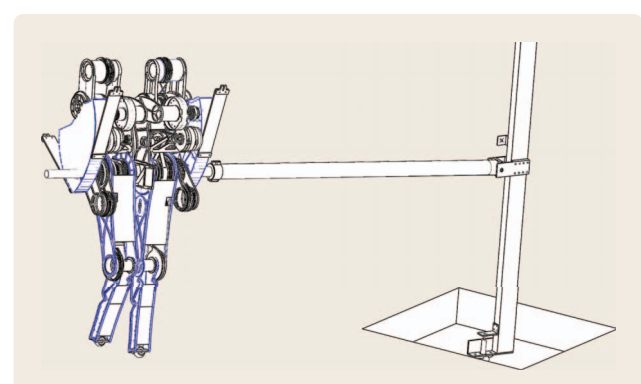


FIGURE 2 Approximate planar motion. The boom constrains MABEL's motion to the surface of a sphere centered at the attachment point of the boom on the central tower. The boom is approximately 2.25 m long. The central tower is supported on a slip ring through which power and digital communication lines, such as E-stop and Ethernet, are passed.

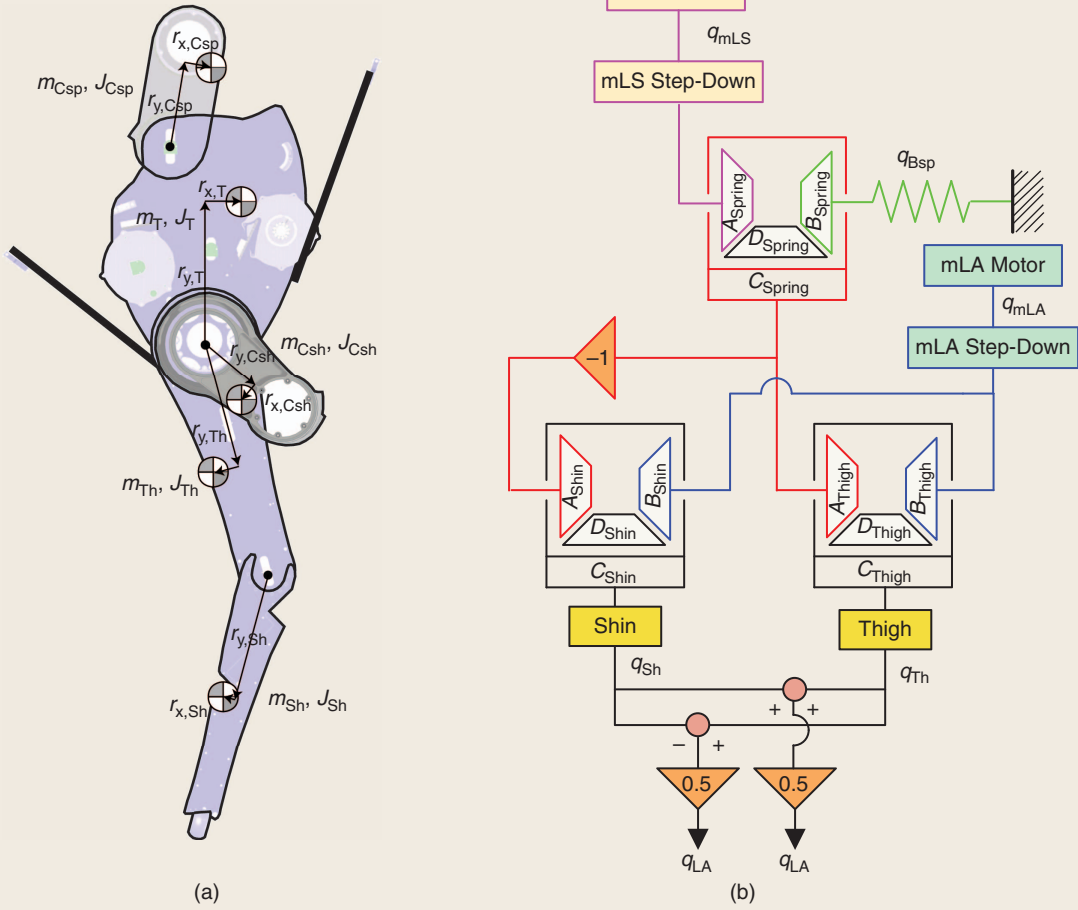


FIGURE 3 Robot and transmission mechanism. (a) Links comprising MABEL. Csp, T, Csh, Th, and Sh denote C_{Spring} , Torso, C_{Shin} , Thigh, and Shin, respectively. (b) The transmission mechanism consists of spring, thigh, and shin differentials. The spring differential realizes a serial connection between the leg-shape motor and the spring. The thigh differential moves the thigh link in the leg, while the shin differential moves the shin link. The gear ratios are described in figures 6 and 7.

Transmission

The transmission mechanism for each half of MABEL consists of three cable differentials, labeled the spring, thigh, and shin differentials, and a spring, as shown in Figure 3(b). The thigh and shin differentials translate shin angle and thigh angle into leg shape and leg angle. Thus, the electric motors control the leg angle and leg shape. The spring differential forms a series connection between a spring and the motor for leg shape so that the resulting system behaves approximately like a pogo stick.

To keep the legs light, the motors and differentials are mounted in the torso. Instead of the gear differentials depicted in Figure 5, cable differentials are used to achieve low friction and backlash. Although cable differentials and gear differentials have different assemblies, they work in the same manner. Each consists of three components, labeled A , B , and C , connected by an internal, unobserved, idler D . When the gear ratios are all equal, the components

A and B are constrained such that the average motion of the two is equal to the motion of the component C . Consequently, A and B can move in opposite directions if C is held stationary, and the motion of C is half of A if B is held stationary. In other words, $(q_A + q_B)/2 = q_C$ and $(q_A - q_B)/2 = q_D$, where q_A , q_B , q_C , and q_D denote the angular displacements of the components.

In MABEL's transmission mechanism, A and B are inputs to the differential, while C is an output. In the following, A_{Shin} , B_{Shin} , and C_{Shin} refer to the components A , B , and C of the shin differential and likewise for the remaining two differentials. C_{Thigh} and C_{Shin} in Figure 3(b) are attached to the thigh and shin links, respectively. The pulleys B_{Thigh} and B_{Shin} are both connected to the leg-angle motor. The pulleys A_{Thigh} and A_{Shin} are connected to the pulley C_{Spring} , which is the output pulley of the spring differential. The spring on each side of the robot is implemented with two fiberglass

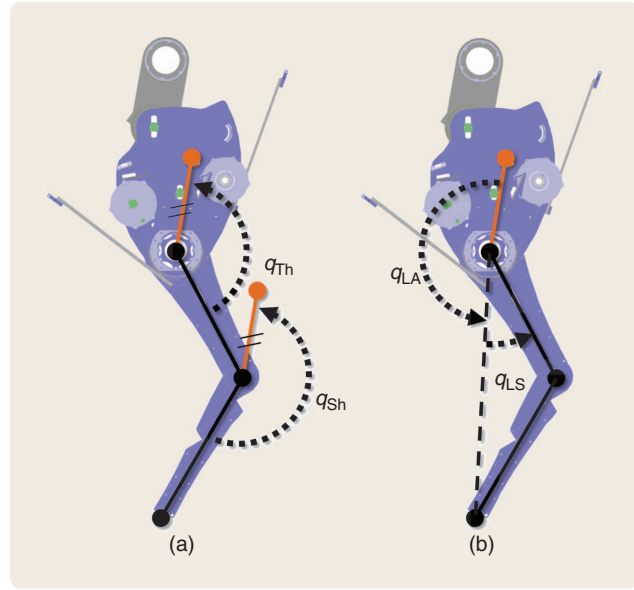


FIGURE 4 Actuated coordinates. (a) shows a more conventional choice of actuated coordinates. The actuated coordinates on MABEL, shown in (b), correspond to controlling the length and orientation of the virtual prismatic leg indicated by the dashed line connecting the toe to the hip. The counterclockwise direction is positive.

plates connected in parallel to the differentials through cables, as shown in Figure 1. Due to the cables, the springs are unilateral, meaning they can compress but not extend; this aspect is discussed below.

Figures 6 and 7 illustrate how this transmission works when one of the coordinates q_{LA} or q_{LS} is actuated, while the other coordinate is held fixed. The path from spring displacement to rotation in q_{LS} is similar. The net motion in q_{LS} from the leg-shape motor and the spring is the sum of the individual motions.

Variable Names

To name the variables appearing in the robot, we use the index set

$$\mathcal{I} = \{mLS_L, mLA_L, mLS_R, mLA_R\}, \quad (3)$$

where the subscripts L and R mean left and right, mLS means motor leg shape, and mLA means motor leg angle; see Figure 3(b). For the links, we define the index set

$$\mathcal{L} = \{T, Csp, Th, Sh, Csh, Boom\}, \quad (4)$$

where T, Csp, Th, Sh, Csh, and Boom represent Torso, C_{Spring} , Thigh, Shin, C_{Shin} , and Boom, respectively, as depicted in Figure 3(a). For the transmission mechanism, we define the index set

$$T = \{Asp, Bsp, Dsp, Ath, Bth, Dth, Ash, Bsh, Dsh, mLSSd, mLAsd, mLS, mLA\}, \quad (5)$$

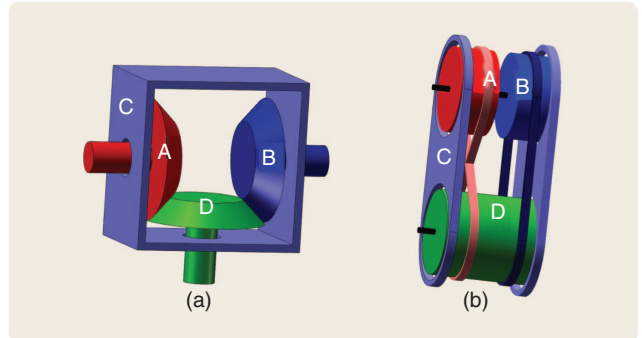


FIGURE 5 Two versions of a differential mechanism. (a) shows a conventional gear differential, while (b) shows a cable differential. Each differential consists of three components, labeled A, B, and C, connected by an internal, unobserved, idler D. In (a), A, B, and D are gears, while in (b), they are pulleys. In both (a) and (b), C is a link. The kinematic equations for a differential are given by $(q_A + q_B)/2 = q_C$ and $(q_A - q_B)/2 = q_D$, assuming equal gear ratios, where q_A , q_B , q_C , and q_D denote the angular displacements of the components.

where A, B, and D correspond to the components of the differentials in Figure 3(b), and sp, th, sh, and sd denote spring, thigh, shin, and step down, respectively, as depicted in Figure 3. Throughout this article, the notation for coordinates and torques in Table 1 is used.

Sensors

MABEL is equipped with encoders and contact switches, but not force sensors. On each side of the robot, magnetic encoders for measuring joint angles are present on the pulleys mLA, mLS, Dth, Bsp, and mLAsd, as well as the knee joint. From the geometry of the legs, the leg-shape angle q_{LS} is one half of the knee joint angle. Each encoder has a resolution of 2048 counts per revolution and thus 0.1758 deg/count.

The angle of the thigh with respect to the torso is measured by an encoder that has 2048 counts per revolution and a 19.8:1 gear ratio, for a total of 40,550.4 counts per revolution and thus 0.008878 deg/count. The angle of the torso with respect to the vertical is measured by an encoder that has 2048 counts per revolution and a 3:1 gear ratio, for a

TABLE 1 Notation for MABEL's coordinates and torques. The subscripts L and R denote the left leg and right leg, respectively.

$q_{LS_{L,R}}$	Leg-shape angle
$q_{mLS_{L,R}}$	Motor leg-shape angle
$q_{LA_{L,R}}$	Leg-angle angle
$q_{mLA_{L,R}}$	Motor leg-angle angle
$q_{Bsp_{L,R}}$	Pulley- B_{Spring} angle
$T_{mLS_{L,R}}$	Leg-shape motor torque
$T_{mLA_{L,R}}$	Leg-angle motor torque
$T_{Bsp_{L,R}}$	Pulley- B_{Spring} torque

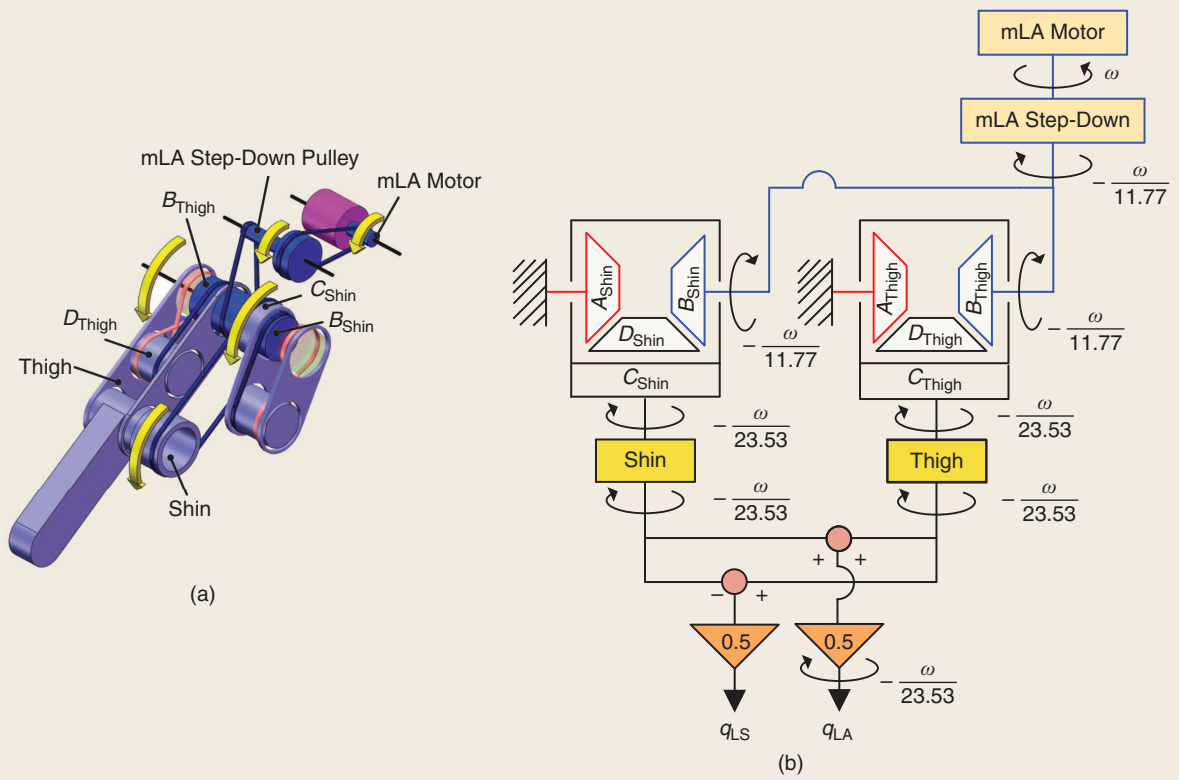


FIGURE 6 Leg-angle actuation: (a) q_{LA} pulley system and (b) q_{LA} transmission. Torque from the leg-angle motor is transmitted to q_{LA} as defined in Figure 4 through one step-down pulley and two differentials, thigh and shin. (b) uses gear differentials to depict the actuation of q_{LA} , with the indicated gear ratios.

total of 6144 counts per revolution and thus 0.05859 deg/count. The pitch angle of the boom is measured by an encoder with 2048 counts per revolution and a 17.6:1 gear ratio, for a total of 36,044.8 counts per revolution and thus 0.09988 deg/count. The rotation angle of the central tower is measured by an encoder with 40,000 counts per revolution and a 7.3987:1 gear ratio, for a total of 295,948 counts per revolution, and thus 0.001216 deg/count.

To detect impacts with the ground, two contact switches are installed at the end of each leg. Ground contact is declared when either of the two switches closes. Additional contact switches are installed at the hard stops on various pulleys to detect excessive rotation within MABEL's workspace. If a contact switch on a hard stop closes, power to the robot is immediately turned off by the computer.

Because MABEL does not have velocity sensors, angular velocities must be estimated by numerically differentiating position signals. For real-time applications, such as feedback control, causal methods for numerical differentiation are required [24], [25]. For offline applications, such as parameter identification, acausal or smoothing algorithms can be employed [26]. We use the spline interpolation method of [27], which can be used in a causal or acausal manner.

Embedded Computer and Data Acquisition

The onboard computer is a 1.3-GHz Intel Celeron M CPU running a QNX real-time operating system. The RHexLib library, originally developed for the robot RHex [28], is used for implementing control-algorithm modules as well as for logging data over the network data and communicating with the robot. A user interface for monitoring the robot's state on a secondary Linux-based system uses utilities provided by RHexLib.

Digital and analog IO are handled with compactPCI data-acquisition cards from Acromag. A custom-built compactPCI module houses the interface circuitry between the Acromag data-acquisition cards and the sensors on the robot.

The sample period of the embedded controller is set at 1 ms. Though a 1.5-ms sample period is probably adequate, the power to the robot is automatically shut off by a watchdog timer if any controller update cycle exceeds 1 ms. Data acquisition and logging consume approximately 0.5 ms of each sample period, leaving 0.5 ms for control computations and signal processing. PD-based controllers can be implemented in the available processing time without special programming considerations. For controllers based on inverse dynamics, such as those reported in [9], the

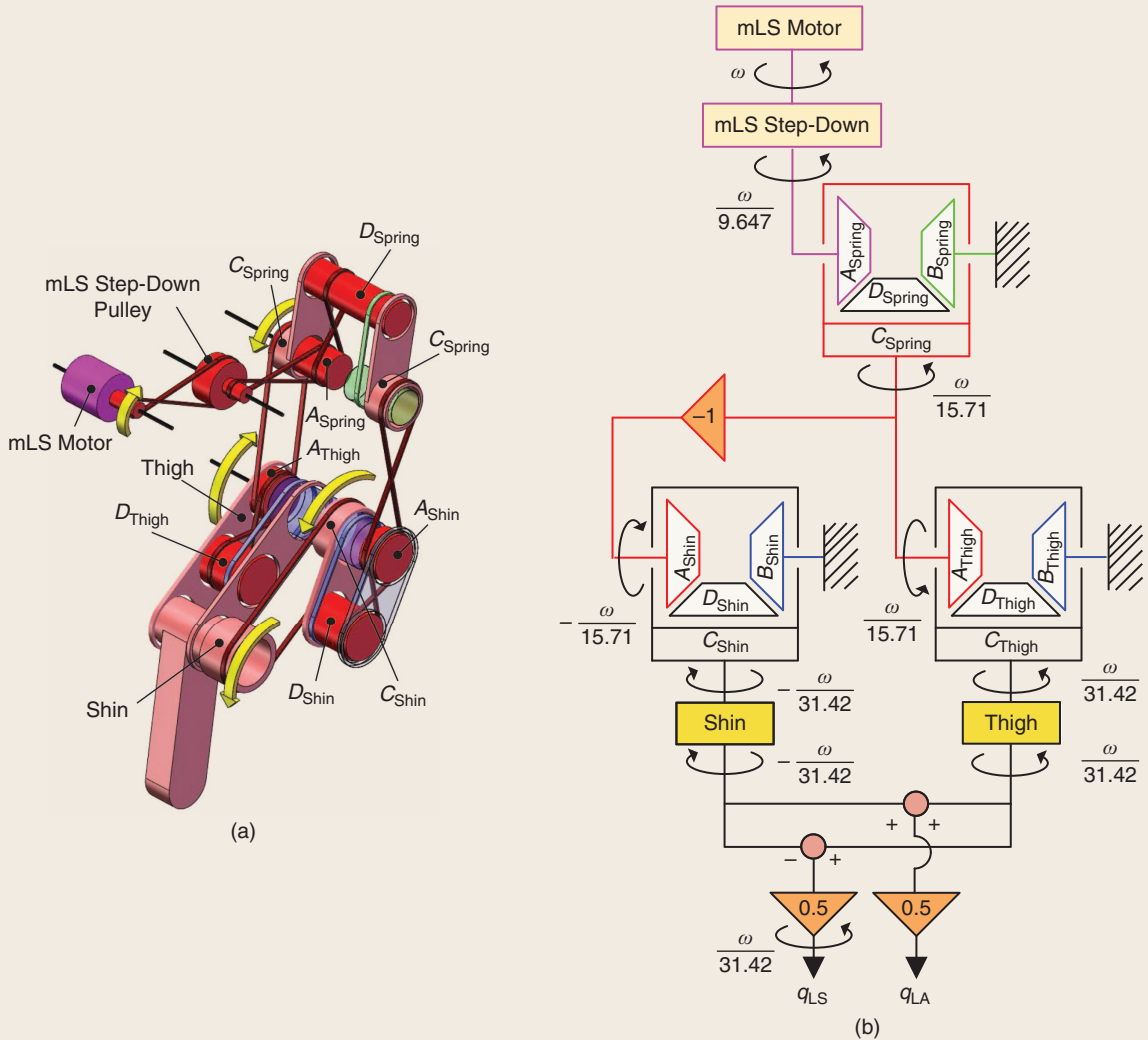


FIGURE 7 Leg-shape actuation: (a) q_{ls} pulley system and (b) q_{ls} transmission. Torque from the leg-shape motor is transmitted to q_{ls} as defined in Figure 4 through one step-down pulley and three differentials, spring, thigh, and shin. (b) uses gear differentials to depict the actuation of q_{ls} , with the indicated gear ratios.

real-time calculations are performed in approximately 0.11 ms with a public-domain C++-template library from Boost [29], which provides standard matrix-algebra operations.

PARAMETER IDENTIFICATION PROCEDURE

CAD packages provide estimates of the masses of the links and pulleys comprising MABEL, their lengths and radii, centers of mass, and moments of inertia. If we also account for the location and mass distribution of items not normally represented in a CAD drawing, such as ball-bearing shape and density, the length and density of pulley cables, electrical wiring, onboard power electronics, and actuators and sensors, then the mechanical parameters of the robot can be estimated. Consequently, one goal of the identification procedure is to validate these estimates by comparing predicted responses to experimental data.

In addition, model parameters for which reliable estimates are not available from CAD drawings include motor torque constants, rotor inertias, spring stiffness, and preload. Finally, friction parameters cannot be estimated by a CAD program and must be determined experimentally. The parameters to be identified are shown in Table 2.

Steps in the Identification Process

The first phase of the identification process focuses on estimating the actuator and friction parameters in the transmission, as well as validating the pulley inertia estimates provided by the CAD program. The torque constant K_t and rotor inertia J_{rotor} of each motor are also determined by analyzing the motors in series with a chain of known inertias formed by selectively coupling the pulleys that form the three differentials, as shown in figures 6 and 7. Because

TABLE 2 Parameters to be identified, where $i \in \mathcal{I}$, $\ell \in \mathcal{L}$, and $t \in \mathcal{T}$. The subscripts L and R denote the left leg and right leg, respectively.

Differentials and Motors	
K_i	Motor torque constant
$J_{\text{rotor}, i}$	Inertia of the rotor
J_t	Inertia of the transmission pulleys
μ_i	Friction coefficient
b_i	Motor bias
Thigh and Shin (Leg)	
m_ℓ	Mass of the link ℓ
J_ℓ	Inertia of the link ℓ
$m_\ell r_{x, \ell}$	Center of mass in the x-direction of the link ℓ multiplied by mass of the link ℓ
$m_\ell r_{y, \ell}$	Center of mass in the y-direction of the link ℓ multiplied by mass of the link ℓ
Compliance (Spring)	
$K_{B_{\text{L,R}}}$	Spring stiffness
$Kd_{B_{\text{L,R}}}$	Spring damping coefficient
$K_{C,i}$	Cable stretch stiffness
$Kd_{C,i}$	Cable stretch damping coefficient

the pulleys are connected by low-stretch steel cables to form a one-degree-of-freedom system, various paths in the transmission mechanism can be modeled by lumping the moments of inertia of the pulleys. This lumped moment of inertia can be calculated by the CAD model and added to the rotor inertia of the motor. In addition, this lumped moment of inertia can be obtained from experiments. These data can be used to estimate motor torque constants, rotor inertias, viscous friction, and motor torque biases.

Next, the legs are coupled to the transmission to validate the actuation-transmission model in conjunction with the center of mass and moments of inertias of the links constituting the thigh and shin, as provided by the CAD model. For these experiments, the compliance is removed from the system by locking the orientation of the pulley B_{Spring} ; the torso is held in a fixed position as well. Following this experiment, the torso's inertial parameters are estimated for validation.

Compliances are determined last. Two sources of compliance are present in the robot. One source is the unilateral, fiberglass spring designed into the transmission. The other source, which is unplanned, arises from stretching of the cables between the pulleys. The compliance of the unilateral spring is obtained from static experiments, and the compliance due to cable stretch is estimated from dynamic experiments that apply high torques to the robot.

Experimental Setup for the Motor, Differential, and Leg Parameters

The first phase of the identification process uses the setup depicted in Figure 8. The torso is fixed relative to the world frame, and the legs can freely move. The position of the pulley B_{Spring} is fixed as well, removing compliance for the initial identification phase. Torque commands are recorded and sent to the amplifiers. In turn, the amplifiers regulate the currents in the motor windings, thereby setting the motor torque values. The rotation of the motors is transmitted to the thigh and shin links through the transmission differentials as shown in figures 6–8.

The leg angles q_{LA} and q_{LS} are related to the corresponding motor angles and the angle of the pulley B_{Spring} by

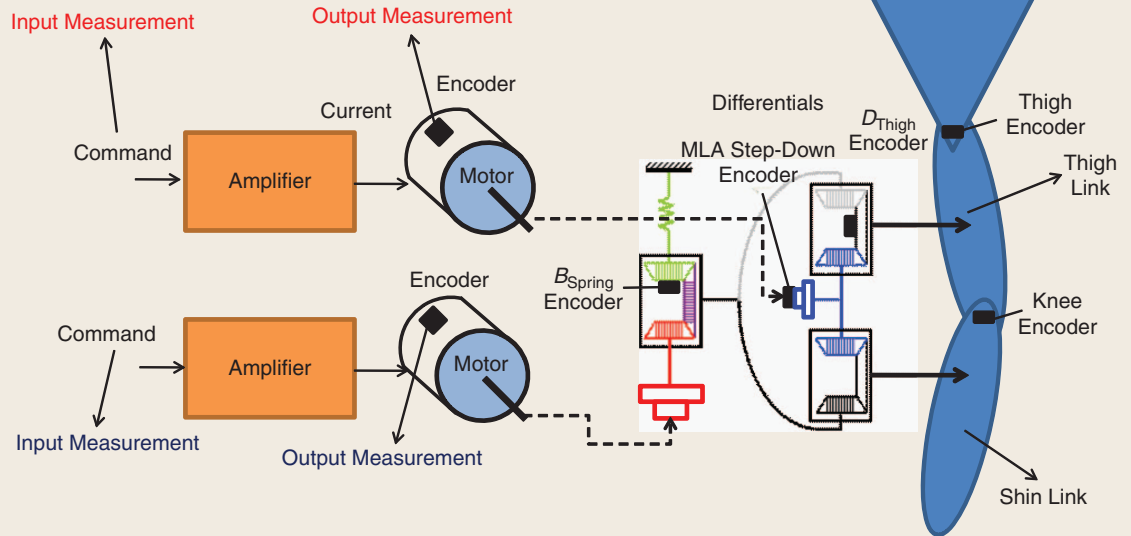


FIGURE 8 Experimental setup for parameter identification. Motor commands are logged as the input, while the encoder signals for the motor angles, the pulleys C_{Thigh} and D_{Thigh} , and the knee-joint angle are saved as outputs.

We take advantage of the modular nature of the robot to design experiments that allow us to sequentially build the model element by element, estimating only a few parameters at each stage of the process.

$$q_{LA} = \frac{1}{\gamma_{LA \rightarrow mL}} q_{mLA} \quad (6)$$

and

$$q_{LS} = \frac{1}{\gamma_{LS \rightarrow mL}} q_{mLS} + \frac{1}{\gamma_{LS \rightarrow Bsp}} q_{Bsp}, \quad (7)$$

where $\gamma_{LS \rightarrow mL} = 31.42$, $\gamma_{LA \rightarrow mL} = -23.53$, and $\gamma_{LS \rightarrow Bsp} = 5.18$ are the gear ratios from LS to mL, from LA to mL, and from LS to Bsp. The calculated angles q_{LS} and q_{LA} are also logged during the experiments.

Relations (6) and (7) hold under the assumption that the cables do not stretch, which is the approximation made here, because no external loads are applied to the legs or the pulleys. When the robot is walking, the transmission system is heavily loaded due to the weight of the robot, and cable stretching occurs. This behavior is observed by the violation of relations (6) and (7). Cable stretch is taken into account in the last step of the identification process.

It is typical for power amplifiers to exhibit a small bias in the commanded current, which in turn causes bias in the motor torques. Before beginning system identification, these biases are estimated and compensated for each motor following the procedure described in "How to Estimate Motor-Torque Biases."

TRANSMISSION IDENTIFICATION

For system identification, the fact that the differentials in the transmission are realized by a series of cables and pulleys is an advantage because we can select how many pulleys are actuated by disconnecting cables. For each pulley combination, the lumped moment of inertia can be computed. Therefore, if the electrical dynamics of the motor and power amplifiers are neglected, the lumped pulley system can be modeled as the first-order system

$$J_{lumped}\dot{\omega} + \mu_{lumped}\omega = u, \quad (8)$$

where J_{lumped} is the lumped moment of inertia, μ_{lumped} is the lumped friction coefficient, ω is the angular velocity of the motor, and u is the commanded motor torque. By identifying J_{lumped} and μ_{lumped} for three different combinations of pulleys plus motor, it is possible to determine K_T and J_{rotor} , as well as confirm the lumped pulley inertia predicted by the CAD model. For each side of the robot, the three pulley combinations of Figure 9(a) are used for the

leg-angle path, while the three pulley combinations of Figure 9(b) are used for the leg-shape path.

Motor Torque Correction Factor and Inertia Correction Factor

The leg-angle-identification experiments are performed successively on the leg-angle motor in combination with one, three, and five pulleys as shown in Figure 9(a). The leg-shape-identification experiments are performed

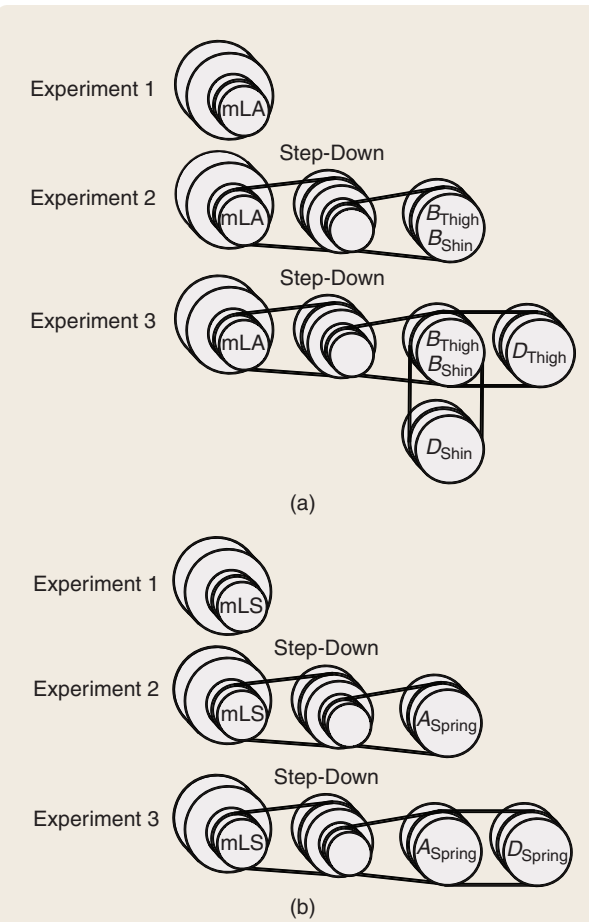


FIGURE 9 Pulley choices for identifying the transmission parameters. (a) q_{LA} path and (b) q_{LS} path. The various pulley combinations are formed by selectively disconnecting cables in the transmission. If the inertias of the pulleys are known, then two pulley combinations are sufficient to identify the inertia of the motor rotor and the torque constant. By adding a third pulley combination, the pulley inertias provided by the CAD program can be validated.

How to Estimate Motor-Torque Bias

In normal operation of the robot, the commanded motor torques may vary from -10 to 10 N-m or higher, in which case a bias of 0.1 N-m in the commanded torque is insignificant. We are using the pulleys comprising the differentials as a known load when identifying the motor characteristics. Because the pulleys have low inertia as shown in Table 3, the commanded motor torques are approximately 1 N-m, in which case a torque bias of 0.1 N-m is significant.

For each parameter estimation experiment, the motor-torque biases are estimated and removed by the following procedure. First, to minimize the effect of friction from the remaining pulleys, each motor pulley is isolated by disconnecting the cable between the motor and the rest of the transmission. Each motor is actuated with a zero-mean sinusoidal torque command. An amplifier bias is expected to cause the motor position to drift slowly, as shown in Figure S1. Differentiating the measured motor position gives the angular velocity, as shown in Figure S2.

The transfer function between the torque input and the angular velocity can be modeled as a first-order system, similar to (8), with an additional step input. Identification of the bias is therefore accomplished with the two-input, first-order autoregressive model [S1, pp. 71–73]

$$y_k = a_1 y_{k-1} + b_1 u_{1,k-1} + b_2 u_{2,k-1}, \quad (\text{S1})$$

where y is the motor angular velocity, u_1 is the commanded motor torque, and u_2 is a sequence of ones. Rearranging (S1) gives

$$y_k = a_1 y_{k-1} + b_1(u_{1,k-1} + b_2/b_1). \quad (\text{S2})$$

The bias is removed by subtracting b_2/b_1 from the commanded motor torque.

REFERENCES

- [S1] L. Ljung, *System Identification: Theory for the User*, 1st ed. Upper Saddle River, NJ: Prentice-Hall, 1986, pp. 71–73.

successively on the leg-shape motor in combination with one, three, and five pulleys as shown in Figure 9(b). The lumped moments of inertia of each combination, including the contributions of the cables can be expressed as

$$J_i = J_{\text{rotor}} + J_{\text{pulley},i} + J_{\text{cable},i}, \quad i = 1, 2, 3, \quad (9)$$

where i denotes experiment number, J_{rotor} is the inertia of the motor rotor, $J_{\text{pulley},i}$ is the lumped moment of inertia of the pulley combination for experiment i , which is obtained by combining the pulley inertias shown in Table 3 with the gear ratios between the pulleys taken into account, and $J_{\text{cable},i}$ is the lumped cable moment of inertia calculated from the mass of the cable per unit length and the length of the cable, with gear ratios taken into account.

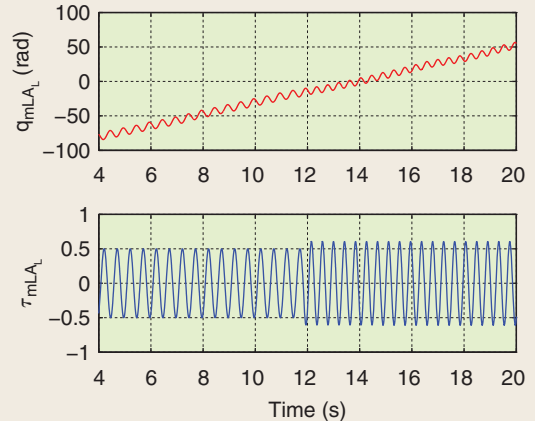


FIGURE S1 Amplifier bias. A zero-mean command input to the amplifier produces a motor position output that slowly drifts with time, showing that the amplifier is biased. The drift is independent of the input amplitude and frequency.

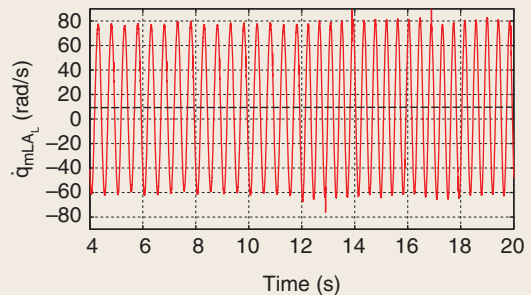


FIGURE S2 Differentiated output. The mean value of the differentiated signal, which is given by the dashed line, is nonzero.

Letting $J_{\text{rotor, man}}$ denote the value of the rotor inertia supplied by the manufacturer, we define the scale factor α_{rotor} by

$$\alpha_{\text{rotor}} = \frac{J_{\text{rotor}}}{J_{\text{rotor, man}}}, \quad (10)$$

which we seek to estimate. In a similar manner, we define the scale factor α_{torque} for the motor by

$$\alpha_{\text{torque}} = \frac{K_T}{K_{T, \text{man}}}, \quad (11)$$

where $K_{T, \text{man}}$ is the value of the motor torque constant supplied by the manufacturer and K_T is the true motor torque constant. In each experiment, the commanded motor torque

is calculated by multiplying the current commanded by the power amplifier by $K_{T,\text{man}}$. As illustrated in Figure 10, it follows that the transfer function from the commanded motor torque to the measured motor angular velocity is a scalar multiple of (8). Hence, the moment of inertia from the experiments is related to the moment of inertia of (9) by

$$J_{\exp,i} = \alpha_{\text{torque}} (\alpha_{\text{rotor}} J_{\text{rotor, man}} + J_{\text{pulley},i} + J_{\text{cable},i}), \quad i = 1, 2, 3, \quad (12)$$

where $J_{\exp,i}$ is the lumped moment of inertia estimated on the basis of the i th experiment.

Three moment of inertia estimates, denoted by $J_{\exp,1}$, $J_{\exp,2}$, and $J_{\exp,3}$, respectively, are obtained from each of the leg-shape and leg-angle experiments. Arranging the equations for each set of experiments in matrix form gives

$$\Psi = \Gamma \begin{bmatrix} \alpha_{\text{torque}} \alpha_{\text{rotor}} \\ \alpha_{\text{torque}} \end{bmatrix}, \quad (13)$$

where

$$\Psi = \begin{bmatrix} J_{\exp,1} \\ J_{\exp,2} \\ J_{\exp,3} \end{bmatrix}, \quad \Gamma = \begin{bmatrix} J_{\text{rotor, man}} & J_{\text{pulley},1} + J_{\text{cable},1} \\ J_{\text{rotor, man}} & J_{\text{pulley},2} + J_{\text{cable},2} \\ J_{\text{rotor, man}} & J_{\text{pulley},3} + J_{\text{cable},3} \end{bmatrix}.$$

The estimates of α_{torque} and α_{rotor} are then obtained by least squares fit

$$\begin{bmatrix} \alpha_{\text{torque}} \alpha_{\text{rotor}} \\ \alpha_{\text{torque}} \end{bmatrix} \triangleq (\Gamma^T \Gamma)^{-1} \Gamma^T \Psi. \quad (14)$$

TABLE 3 Moments of inertia of the pulleys in the transmission as obtained from the CAD model.

Pulley	Moment of Inertia (kg·m ²)
J_{mLS}	9.0144e-4
J_{mLA}	4.4928e-4
$J_{\text{A}\theta}$	1.6680e-3
$J_{\text{B}\theta}$	2.2181e-3
$J_{\text{D}\theta}$	1.0826e-3
$J_{\text{A}\phi}$	1.6974e-3
$J_{\text{B}\phi}$	2.2181e-3
$J_{\text{D}\phi}$	2.0542e-3
$J_{\text{A}\psi}$	2.3464e-3
$J_{\text{B}\psi}$	1.8686e-3
$J_{\text{D}\psi}$	1.9313e-3
J_{mLSSd}	2.7117e-3
J_{mLASd}	1.0950e-3

Experimental Results

Inputs for identification are designed as follows. Starting from 0.5 Hz, the input frequency is increased in 17 steps to 50 Hz. To allow the system response to reach steady state, each frequency is held constant for ten periods until changing to the next higher frequency. At each frequency increment, the magnitude is also incremented to prevent the measured motor angular velocity from becoming too small. Figure 11 illustrates the input signal and corresponding system response. The Matlab System Identification Toolbox is used to identify the transfer function (8). Table 4 shows the results obtained from the experiments.

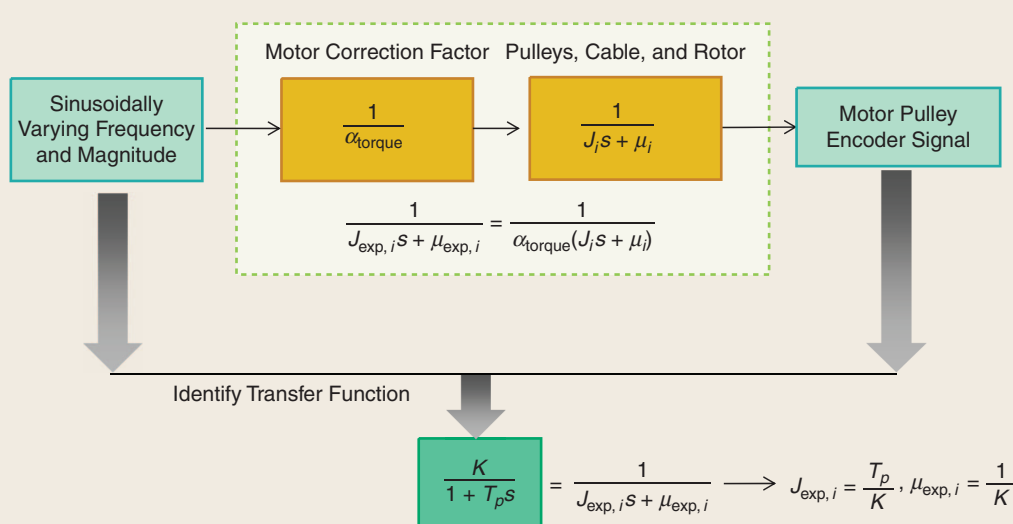


FIGURE 10 Transfer function from the amplifier command input to the motor encoder signal output. The parameter α_{torque} is the correction factor for the motor torque constant supplied by the manufacturer. The measured transfer function is $1/[\alpha_{\text{torque}}(J_i s + \mu_i)]$. The Matlab System Identification Toolbox is used to estimate the first-order transfer function from the measured data.

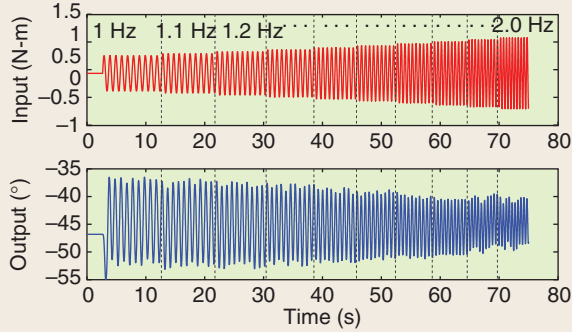


FIGURE 11 Illustrative input and output for system identification. The input is a modified chirp signal, that is, a sinusoid with time-varying frequency and magnitude. Each frequency is held constant until the system reaches steady state.

On the basis of the values in Table 4, α_{torque} and α_{rotor} are calculated by (14). The estimated values are listed in Table 5, along with the motor biases. The scale factors α_{rotor} indicate that the actual rotor inertias of the leg-shape motors are within 7% of the manufacturer's reported values, while the rotor inertias of the leg-angle motors are 25% less than the manufacturer's reported values. The scale factors α_{torque} of the leg-angle motors on the left and right sides of the robot differ by less than 5%. For the leg-shape motors, the large difference in the scale factors α_{torque} is expected. In particular, motors of different characteristics for the left and right sides of the robot were necessary when one of the motors failed early in the construction process and was replaced with a motor from a previous prototype. We also note that motor biases, which range in magnitude from 0.002 to 0.107 N·m, are small in comparison to the torques that are expected in walking experiments, which can exceed 2 N·m for leg angle and 8 N·m for leg shape [9].

For the remainder of this article, the motor torque constant is computed by

$$K_T = \alpha_{\text{torque}} K_{T,\text{man}}.$$

TABLE 4 Identified experimental moments of the inertia and friction coefficients for the transmission mechanism.

		$i=1$	$i=2$	$i=3$
mLS _L	$J_{\text{exp},i}$ (kg·m ²)	8.819e-4	1.099e-3	1.112e-4
	$\mu_{\text{exp},i}$ (N·m·s/rad)	5.655e-3	6.518e-3	7.142e-3
mLA _L	$J_{\text{exp},i}$ (kg·m ²)	5.514e-4	7.223e-4	7.436e-4
	$\mu_{\text{exp},i}$ (N·m·s/rad)	2.332e-3	4.365e-3	3.858e-3
mLS _R	$J_{\text{exp},i}$ (kg·m ²)	1.104e-3	1.360e-3	1.431e-3
	$\mu_{\text{exp},i}$ (N·m·s/rad)	6.545e-3	9.811e-3	9.879e-3
mLA _R	$J_{\text{exp},i}$ (kg·m ²)	5.217e-4	6.900e-4	7.328e-4
	$\mu_{\text{exp},i}$ (N·m·s/rad)	1.718e-3	4.048e-3	4.703e-3

LEG AND TORSO PARAMETERS

Thigh and Shin Links

The thigh and shin links of the legs are actuated by the torque transmitted through the transmission, as shown in figures 3(b) and 8. The total mass, center of mass, and inertia of each link are assumed known from the CAD model; their values are given in Table 6. The values of the motor torque constants and rotor inertias estimated for the transmission are assumed. Friction coefficients may differ from the values estimated for the transmission, however, because the hip and knee joints are now actuated. In this section, the torso continues to be fixed relative to the world frame and the position of the pulley B_{Spring} is fixed as well, removing compliance from the picture.

With the torso fixed, the left and right sides of the robot are, in principle, decoupled; in practice, some coupling of vibration from one side to the other occurs because the test stand is not perfectly rigid, but this coupling is ignored. Choosing the coordinates $q = (q_{\text{mLA}}, q_{\text{mLS}})^T$, the dynamic model for each side can be written in the form

$$D(\theta, \alpha_{\text{rotor}}, q)\ddot{q} + C(\theta, \alpha_{\text{rotor}}, q, \dot{q})\dot{q} + G(\theta, \alpha_{\text{rotor}}, q) = \Gamma_Q, \quad (15)$$

where $D(\theta, \alpha_{\text{rotor}}, q)$, $C(\theta, \alpha_{\text{rotor}}, q, \dot{q})$, and $G(\theta, \alpha_{\text{rotor}}, q)$ are the inertia matrix, Coriolis matrix, and gravity vector, respectively. Moreover, θ is the vector of mechanical parameters from the CAD model, the rotor inertia correction factors α_{rotor} are from Table 5, and the vector Γ_Q of generalized forces acting on the robot, consisting of motor torque and viscous friction, is given by

$$\Gamma_Q = u_{\text{mLA}} + u_{\text{mLS}} - \mu_{\text{mLA}}\dot{q}_{\text{mLA}} - \mu_{\text{mLS}}\dot{q}_{\text{mLS}}. \quad (16)$$

The friction coefficients μ_{mLA} and μ_{mLS} are to be estimated.

Two types of experiment are performed, single-input, single-output (SISO) and multi-input, multi-output (MIMO). Each experiment is performed on one leg at a time. In the SISO experiments, one degree of freedom is actuated and logged, either q_{mLS} or q_{mLA} , while the other degree of freedom is mechanically locked. In the MIMO experiment, both q_{mLS} and q_{mLA} are actuated and recorded. The objective of the SISO

TABLE 5 Motor parameters. The rotor inertias $J_{\text{rotor,man}}$ and torque constants $K_{T,\text{man}}$ are provided by the manufacturer. The correction factors α_{rotor} and α_{torque} as well as the motor biases b are estimated from experimental data.

	mLS _L	mLA _L	mLS _R	mLA _R
$J_{\text{rotor,man}}$ (kg·m ²)	8.755e-4	4.880e-4	8.755e-4	4.880e-4
$K_{T,\text{man}}$ (N·m/A)	1.516	0.577	1.516	0.577
α_{rotor}	0.934	0.741	0.930	0.763
α_{torque}	0.995	1.332	1.287	1.269
b (N·m)	-0.1076	-0.04652	0.02995	-0.001672

TABLE 6 Mass, center of mass, and moment of inertia of the links obtained from the CAD model. The center of mass coordinates r_x and r_y for the robot are defined in Figure 3(a), while the moment of inertia is defined about the joint that passes through the origin of the corresponding link in Figure 3(a). For the boom, the coordinate r_y is measured from the central tower to the robot, while the coordinate r_x is zero.

Link	Mass (kg)	Center of Mass [r_x , r_y] (m)	Moment of inertia (kg-m ²)	Length (m)
Spring (Csp)	1.8987	[0.0009406, 0.1181]	0.04377	—
Torso (T)	40.8953	[0.01229, 0.18337]	2.3727	—
Cshin (Csh)	1.6987	[0.0004345, 0.08684]	0.03223	—
Thigh (Th)	3.2818	[0.0003110, 0.1978]	0.1986	0.5
Shin (Sh)	1.5007	[0.0009671, 0.1570]	0.08813	0.5
Boom	7.2575	[0.0, 1.48494153]	20.4951	2.25

experiments is to estimate the friction parameters in (16). The objective of the MIMO experiment is to validate the model (15), with the parameters obtained from the SISO experiment.

The commanded motor torque is a modified chirp signal plus a constant offset, similar to the transmission identification experiments. The magnitude and offset of the input signal must be selected to keep the links within the robot's work space.

With all the parameters in the model (15) specified, the response of the system excited by the input used in the experiments can be simulated, as shown in Figure 12. The friction parameters μ are estimated by minimizing the cost function

$$J(\mu) = \sqrt{\sum (y_{\text{exp}} - y_{\text{sim}}(\mu))^2}, \quad (17)$$

where y_{exp} is the vector of experimentally measured data, y_{sim} is the vector of simulated data, and μ is the vector of viscous-friction coefficients. As shown in Table 7, the values of μ estimated in this manner are larger than the values from the transmission experiments but not greatly different from those values.

In the MIMO simulations, we observe that variations in the assumed actuator bias of 0.1 N-m, which can be ignored when the legs are supporting the robot, can cause large deviations in the system response when the legs are not supporting the robot. Therefore, for the MIMO simulations, in place of the bias values estimated from the transmission identification, we use the values that minimize the cost function

$$J(b) = \sqrt{\sum (y_{\text{exp}} - y_{\text{sim}}(b))^2}, \quad (18)$$

where y_{exp} is the vector of experimentally measured data, y_{sim} is the vector of simulated data, and b is the bias vector.

The comparisons between simulated and experimental results are presented in figures 13 and 14. All figures show q_{LS} and q_{LA} computed from q_{mLS} and q_{mLA} because the body coordinates q_{LS} and q_{LA} are easier to interpret than the motor positions. It is emphasized that the parameters are either from the transmission identification experiments

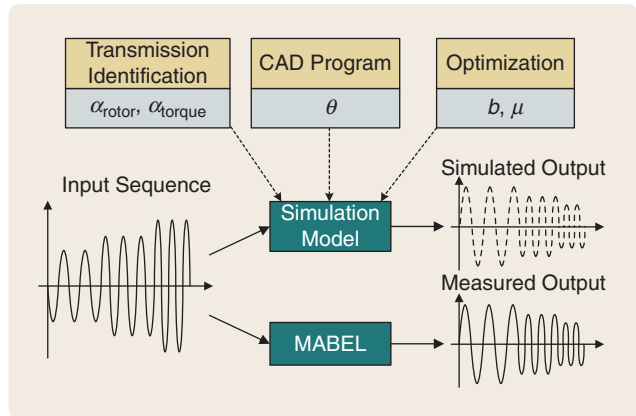


FIGURE 12 Simulation and validation procedures for leg identification. Identical input sequences are applied to the simulation model and MABEL. The simulation model uses the motor parameters estimated from the transmission identification along with the mass-inertia parameters calculated from the CAD program, while torque bias and friction coefficients are free variables used to fit the simulation data to the experimental data. In the validation step, a new input sequence is used and the motor bias is re-estimated, while all remaining parameters are held constant.

or the CAD model, with two exceptions, namely, friction is estimated in the SISO experiments from (17) and used in the MIMO experiments; in the MIMO experiments, motor biases are tuned by (18).

In the SISO experiments, the root mean square (RMS) error varies from 0.69 to 1.1°, while for the MIMO experiments, the RMS error varies from 0.72 to 1.42°. These errors may arise from several sources. For example, the linear

TABLE 7 Estimates of friction coefficients μ and motor biases b obtained by minimizing the costs in (17) and (18), respectively.

	$i = \text{mLS}_L$	$i = \text{mLA}_L$	$i = \text{mLS}_R$	$i = \text{mLA}_R$
μ_i (N-m-s/rad)	9.844e-3	4.316e-3	9.027e-3	4.615e-3
b_i (N-m)	-8.417e-3	2.597e-2	-1.446e-2	-2.461e-3

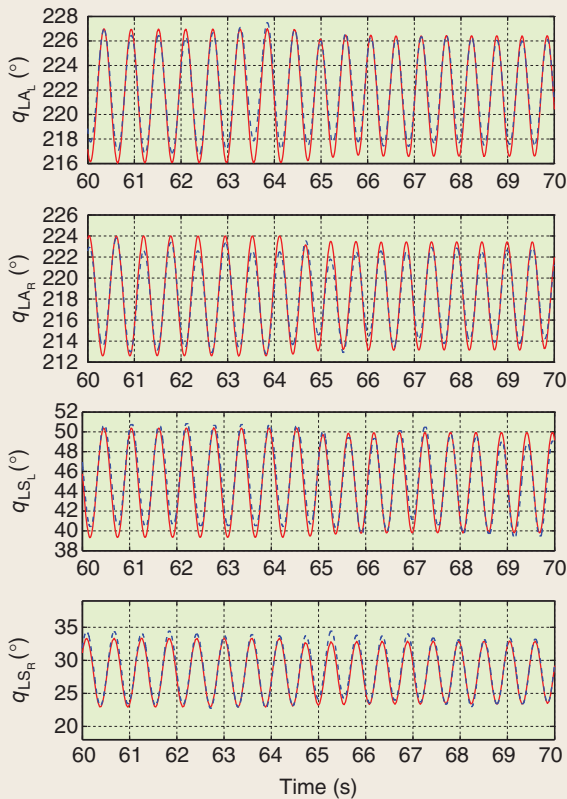


FIGURE 13 Single-input, single-output simulation and experimental data. The joint positions for the simulation are indicated by solid red lines, while the joint positions for the experiments are indicated by dotted blue lines. These data are obtained from the procedure in Figure 12. The root mean square errors are 0.77, 1.1, 0.76, and 0.69°, respectively.

viscous-friction terms in (16), $\mu_{mLA} \dot{q}_{mLA}$ and $\mu_{mLS} \dot{q}_{mLS}$, do not take into account stick-slip behavior in the low-velocity region. Furthermore, electrical wiring is not included in calculating inertial parameters. In addition, motor bias changes slightly for each experimental trial. Finally, cable stretch is assumed to be negligible.

TORSO

The torso represents approximately 41 kg of the total 65-kg mass of the robot. Consequently, the mass and inertia of the torso strongly affect the dynamics of the robot. In principle, the inertia and mass distribution of the torso can be validated by locking the legs in a fixed position and using the leg-angle motors to oscillate the torso. Attempts at executing this experiment in the test stand failed, since movement of the torso is always translated to the legs.

Therefore, instead of dynamic identification of the torso, static balancing experiments are used to validate the CAD model estimates. In the first experiments, the robot is not constrained. Using local PD controllers, we command a posture where the right leg is extended more than the left leg. The

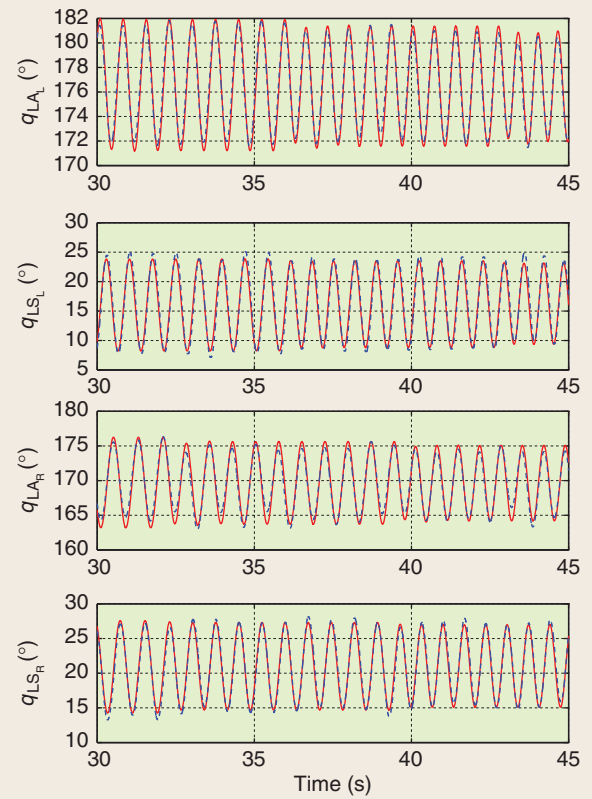


FIGURE 14 Multi-input, multi-output simulation and experimental data. The joint positions for the simulation are indicated by solid red lines, while the joint positions for the experiments are indicated by dotted blue lines. These data are obtained from the procedure in Figure 12. The root mean square errors are 1.0, 1.42, 1.14, and 0.72°, respectively.

robot is then balanced by hand on the right leg. The balance of the robot is maintained with minimal fingertip pressure from one of the experimenters. Once the robot is in a balanced posture, the joint position data are recorded. Many different postures are balanced and logged. From the logged data, we calculate the center of mass position of the robot including the horizontal boom, and we verify that the calculated center of mass is located over the supporting toe.

In a second set of experiments, the position of the hip joint is fixed, with the legs hanging below the robot and above the floor, and with the robot unpowered. The torso is balanced by hand in the upright position. We then calculate the center of mass position of the robot without the boom and check that the center of mass is aligned over the hip joint.

We use ten different postures for the first experiment and seven different postures for the second experiment. Figure 15(a) displays the horizontal distance between the center of mass and the supporting toe for the first experiment, and Figure 15(b) shows the horizontal distance between the center of mass and the hip for the second experiment. We observe that the maximum error is 6 mm,

which is negligible in view of the size of the robot and considering that the experiments are performed with manual balancing. These experiments do not provide information on the vertical position of the center of mass.

COMPLIANCE

The stiffness of the springs that are in series with the leg-shape actuators is estimated by means of static experiments using the calculated spring torques and measured spring deflections. The magnitude of the joint torques used in these experiments is more representative of the torques used in walking [9]. Under these greater loads, the cables in the differentials stretch. This compliance is also modeled.

Spring Stiffness

The series compliance in the drivetrain is now estimated by means of static, constant-torque experiments, performed by balancing the robot on one leg at a time. The setup is illustrated in Figure 16. In these experiments, the torso is no longer locked in place relative to the world frame; it is free. The actuators on one side of the robot are disabled, with the leg on that side folded and tied to the torso. On the other side, a PD-controller is used to maintain the leg angle at 180°, which is straight down. A second PD-controller is used to set the nominal leg shape. An experimenter balances the robot in place with the toe resting on a scale placed on the floor; the experimenter adjusts the overall angle of the robot so that it is exactly balanced on the toe, as when verifying the center of mass of the torso.

With the setup shown in Figure 16, the scale is measuring the combined weight of the robot and the boom. By the design of the differential, when the leg-shape motor holds the pulley A_{Spring} in a fixed orientation, the torque at the pulley C_{Spring} is exactly balanced by the torque at the pulley B_{Spring} . The torque τ_{gravity} at C_{Spring} , shown in Figure 16, is the weight of the robot transmitted through the thigh and shin differentials; its magnitude is given by

$$|\tau_{\text{gravity}}| = \left| \frac{1}{2} W_{\text{robot}} \sin(q_{\text{LS}}) \right|, \quad (19)$$

where W_{robot} is the weight of the robot measured by the scale at the bottom of the foot. The absolute value is used because spring stiffness is positive. The torque τ_{Bsp} at the pulley B_{Spring} , shown in Figure 16, is due to the deflection of the spring and is given by

$$\tau_{\text{Bsp}} = K_{\text{B}} q_{\text{Bsp}}, \quad (20)$$

where K_{B} is the spring stiffness. The spring deflection q_{Bsp} is measured by an encoder installed in the pulley B_{Spring} . The torques τ_{gravity} and τ_{Bsp} , which are related by the differential mechanism, satisfy

$$|\tau_{\text{gravity}}| = 2.59 |\tau_{\text{Bsp}}|. \quad (21)$$

Combining (19)–(21), the spring stiffness is obtained as

$$K_{\text{B}} = \frac{1}{5.18} \left| \frac{W_{\text{robot}} \sin(q_{\text{LS}})}{q_{\text{Bsp}}} \right|. \quad (22)$$

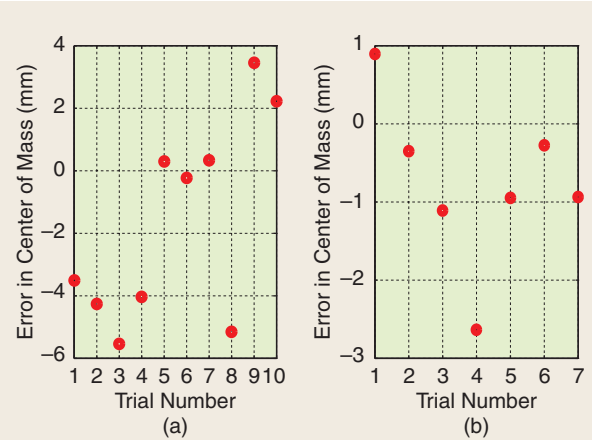


FIGURE 15 Errors in the estimated horizontal position of the center of mass. (a) In these experiments, the robot is manually balanced on one leg, in which case the center of mass of the robot plus the boom must be over the toe. The CAD model provides an estimate of the center of mass. The graph depicts the difference in the measured horizontal component of the center of mass and the CAD-model estimate for ten postures of the robot. The maximum difference is less than 6 mm. (b) In these experiments, the cartesian position of the hip is clamped to a fixed position, with the legs extended below the robot and off the floor. The torso is then balanced in an upright position, providing the horizontal position of the center of mass of the torso. This plot depicts the measured error with respect to the CAD-model estimate for seven trials of the experiment.

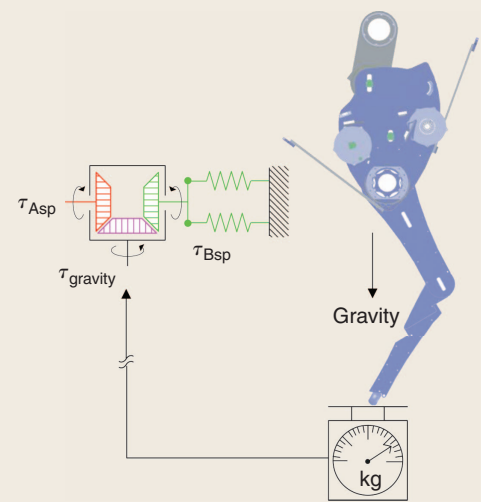


FIGURE 16 Experimental setup for measuring spring stiffness and preload. Pulley A_{Sp} is locked in place by commanding the leg-shape motor to a fixed orientation. Consequently, the torque due to gravity τ_{gravity} must be balanced by the torque from the spring τ_{Bsp} . The resulting spring deflection q_{Bsp} is measured and recorded.

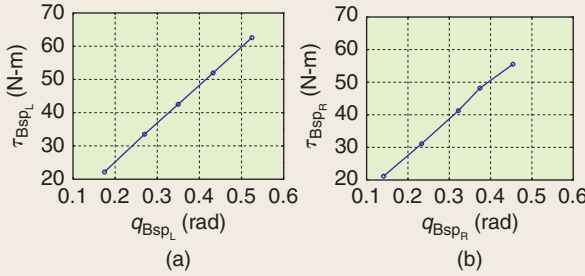


FIGURE 17 Measurements of torque τ_{BSP} versus displacement q_{BSP} obtained from the experimental setup of Figure 16. (a) Left spring and (b) right spring. The data in (a) are fit by $\tau_{BSP_L} = 115.1q_{BSP_L} + 2.214$. The fit shows that, on the left side of the robot, the spring stiffness is 115.1 N-m/rad and the preload offset is 2.214 N-m. On the right side of the robot, the data in (b) are fit by $\tau_{BSP_R} = 111.7q_{BSP_R} + 5.377$, showing that the spring stiffness is 111.7 N-m/rad and the preload offset is 5.377 N-m. The estimated values of spring stiffness and preload are consistent on the left and right sides of the robot.

The design of the experiment is completed by varying q_{LS} over a range of values, here taken to be from 10° to 30° . We emphasize that K_B determined by means of (22) does not depend on the estimated leg-shape motor torque. Indeed, because the spring and motor are connected in series, the torques must balance at the spring differential.

Figure 17 shows the results of performing the above experiments on each leg. Prior to the experiments, it is not obvious if a linear model of the spring deflection would be adequate because the spring folds around the curved torso as shown in Figure 18. From the data, we observe that the spring behavior is nearly linear and that the spring constants for the left and right sides are consistent.

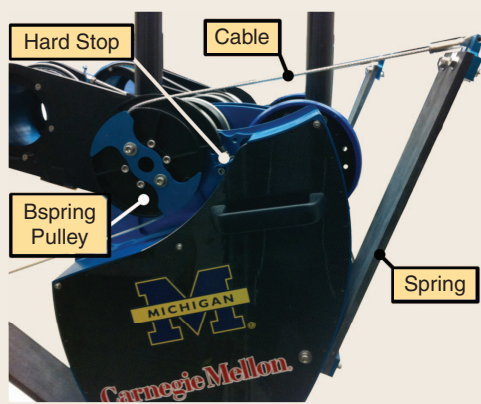


FIGURE 18 MABEL's unilateral springs. The cable, hard stops, and pulley B_{Spring} are also shown. The spring, fabricated from fiberglass plates, is activated when the pulley B_{Spring} rotates and pulls the cable, wrapping the fiberglass plates around the front and back of the torso. The cable cannot push the spring, and hence the spring is unilateral. A rest position is enforced by a hard stop, formed by a stiff spring-damper.

CABLE STRETCH

Experiments reported in [9] show that the cables used in the differentials of MABEL stretch a significant amount under loads typical of bipedal walking. This compliance breaks the relations in (6) and (7). Consequently, q_{LA} and q_{mLA} are independent degrees of freedom, as are q_{LS} , q_{mLS} , and q_{BSP} .

We take into account the stretching of the cables with a spring-damper model. First, relations (6) and (7) are expressed in the form of the constraint

$$c(q) = \begin{bmatrix} q_{mLA} - \gamma_{LA \rightarrow mLA} q_{LA} \\ q_{mLS} - \gamma_{LS \rightarrow mLS} q_{LS} + (\gamma_{LS \rightarrow mLS} / \gamma_{LS \rightarrow BSP}) q_{BSP} \end{bmatrix}, \quad (23)$$

where q is the vector of generalized coordinates for the robot dynamics and $c(q) = 0$ corresponds to no cable stretch. Because the cable-stretch torques act on these constraints, the principle of virtual work yields the input matrix B_{cable} for the cable-stretch torques, given by

$$B_{cable} = \frac{\partial c^T}{\partial q}. \quad (24)$$

Note that we are representing the forces generated in the cables as equivalent torques acting in series with the pulleys in the differentials. We furthermore assume that the cable-stretch torques can be modeled as a linear spring-damper. Therefore, for each side of the robot, the torque from the cable stretch is modeled as

$$\tau_{cable}(q, \dot{q}) = K_C c(q) + Kd_C c(\dot{q}), \quad (25)$$

where K_C is a 2×2 diagonal matrix of spring coefficients, and Kd_C is a 2×2 diagonal matrix of damping coefficients. The spring and damping coefficients of the cables are identified in the next section.

TWO-LEGGED HOPPING FOR FINAL MODEL IDENTIFICATION AND VALIDATION

This section uses a hopping gait to complete the identification of, and subsequently validate, the overall dynamic model of MABEL. While hopping per se is not an objective, the large motor torques employed to launch the robot in the air, in combination with the large ground contact forces at landing, make hopping a convenient means for exciting all of the dynamic modes that are expected to be present when the robot is running on flat ground or walking on uneven ground. Two-legged hopping is chosen over hopping on one leg to simplify the task of obtaining stable hopping.

Dynamic Model

An overall model of the robot is formed by combining the dynamics of the transmission, legs, torso, built-in compliance, and cable stretch. To address hopping, a model of the

The robot is provided information on neither where the step down occurs, nor by how much.

forces between the leg ends and the ground, that is, the ground reaction forces, is also required [30], [31].

The overall dynamic model is derived with the method of Lagrange [10]. When computing the Lagrangian, it is convenient to consider the spring torques, the cable-stretch torques, the ground reaction forces, and the joint-friction torques as external inputs to the model. The generalized coordinates are taken as $q_h := (q_{LA}^L; q_{mLA}^L; q_{LS}^L; q_{Bsp}^L; q_{LA}^R; q_{mLA}^R; q_{LS}^R; q_{Bsp}^R; q_T; p_{hip}^h; p_{hip}^v)$, where, as in figures 3(a) and 4, q_{LA} , q_{mLA} , q_{LS} , and q_{mLS} are the leg angle, leg-angle motor position, leg shape, and leg-shape motor position, respectively; q_T is the angle of the torso with respect to the vertical; and p_{hip}^h and p_{hip}^v are the horizontal and vertical positions of the hip in the sagittal plane. The model is then expressed in second-order form as

$$D_h(q_h) \ddot{q}_h + C_h(q_h, \dot{q}_h) \dot{q}_h + G_h(q_h) = \Gamma_h, \quad (26)$$

where the vector of generalized forces and torques Γ_h acting on the robot is given by

$$\begin{aligned} \Gamma_h = & B_h u + B_{\text{fric}} \tau_{\text{fric}}(q_h, \dot{q}_h) + B_{\text{sp}} \tau_{\text{Bsp}}(q_h, \dot{q}_h) \\ & + \frac{\partial p_{\text{toe}}^T}{\partial q_h} F + B_{\text{cable}} \tau_{\text{cable}}(q_h, \dot{q}_h). \end{aligned} \quad (27)$$

Here, p_{toe} is the position vector of the two leg ends; F is the ground reaction forces on the two legs; and the matrices B_h , B_{fric} , B_{sp} , and B_{cable} , which are derived from the principle of virtual work, define how the actuator torques τ , the joint friction torques τ_{fric} , the spring torques τ_{Bsp} , and the cable-stretch torques τ_{cable} enter the model, respectively.

The model for the unilateral spring is augmented with terms to represent the hard stop, yielding

$$\tau_{\text{Bsp}} = \begin{cases} -K_B q_{\text{Bsp}} - K_d B \dot{q}_{\text{Bsp}}, & q_{\text{Bsp}} > 0, \\ -K_B q_{\text{Bsp}} - K_{d1} q_{\text{Bsp}}^3 - K_{vd1} \dot{q}_{\text{Bsp}}, & q_{\text{Bsp}} \leq 0 \text{ and } \dot{q}_{\text{Bsp}} \geq 0, \\ -K_B q_{\text{Bsp}} - K_{d1} q_{\text{Bsp}}^3 - K_{vd1} \dot{q}_{\text{Bsp}} \\ -K_{vd2} \sqrt{|\dot{q}_{\text{Bsp}}|} \operatorname{sgn}(\dot{q}_{\text{Bsp}}), & q_{\text{Bsp}} \leq 0 \text{ and } \dot{q}_{\text{Bsp}} < 0, \end{cases} \quad (28)$$

where K_B corresponds to the spring constants determined in Figure 17, and where the remaining parameters K_d , K_{d1} , K_{vd1} , and K_{vd2} are to be estimated from hopping data. When $q_{\text{Bsp}} > 0$, the spring is deflected and the model is a linear spring-damper. When $q_{\text{Bsp}} \leq 0$, the pulley is against the hard stop, a stiff damper. This model captures the unilateral nature of MABEL's built-in compliance.

The ground reaction forces at the leg ends are based on the compliant ground model in [30] and [31], using the modifications presented in [32]. The normal force F_n and tangential force F_t acting on the end of each leg are determined by

$$F_n = -\lambda_v^a |z_G|^n \dot{z}_G - \lambda_v^b |z_G|^n \operatorname{sgn}(\dot{z}_G) \sqrt{|\dot{z}_G|} + k |z_G|^n, \quad (29)$$

$$F_t = \mu(d, v) |F_n|, \quad (30)$$

where

$$\dot{d} = v - |v| \frac{\alpha_{h0}}{\alpha_{h0}} d, \quad (31)$$

$$\mu(d, v) = \sigma_{h0} d + \sigma_{h1} \dot{d} + \alpha_{h2} v, \quad (32)$$

when the penetration depth z_G of a leg into the ground is positive and are zero otherwise. The normal force F_n corresponds to a nonlinear spring-damper, with damping coefficient λ_v^a and spring stiffness k_v . According to [30], the exponent n , which depends on the shapes of the surfaces that are in contact, equals 1.5 when the leg end is spherical, which is roughly the case for MABEL. The signed-square-root term on penetration velocity, with coefficient λ_v^b , induces finite-time convergence of the ground penetration depth when the robot is standing still.

The tangential force F_t is in the form of a friction model with variable coefficient of friction μ determined by the LuGre model [31]. The LuGre model represents the interface between the two contacting surfaces as bristles, modeled by springs and dampers, which, if the applied tangential force is sufficient, are deflecting and slipping. The average deflection d of the bristles is the internal state of the friction model, v is the relative velocity of the contacting surfaces, σ_{h1} is the damping coefficient, and α_{h2} is the coefficient of viscous friction. The stiffness of the spring is σ_{h0} and the coefficient of static friction is α_{h0} .

PARAMETERS FOR CABLE STRETCH, HARD STOP, AND GROUND MODELS

A heuristic controller for a hopping gait is given in "How Hopping Is Achieved." Because the cable stretch coefficients are not yet identified, the hopping controller is hand tuned on an approximate simulation model that assumes the cables are rigid; the approximate model also uses the ground reaction parameters from [32]. The tuning process adjusts PD-controller gains and setpoints in the various phases of the gait, with the goal of obtaining sustained hopping. When the controller is implemented on MABEL, steady-state hopping is not achieved, even after extensive trial-and-error tuning in the laboratory. Five hops is typical before the robot falls.

How Hopping Is Achieved

A hopping gait is used to complete the identification of, and subsequently validate, the overall dynamic model of MABEL. A heuristic controller for two-legged hopping is formed by decomposing a hopping gait into its elementary phases, as illustrated in Figure S3. For each phase $X \in \{I, II, III, IV_a, IV_b, V\}$ of Figure S3, the controlled variables are

$$h := \begin{bmatrix} q_{LA_L} \\ q_{mLS_L} \\ q_{LA_R} \\ q_{mLS_R} \end{bmatrix}, \quad (S3)$$

while the reference command h_X^{ref} changes in each phase as given in (S5)–(S17) below. The PD controller

$$u = K_p(h_X^{\text{ref}} - h) + K_d(\dot{h}) \quad (S4)$$

is used, where K_p is a 4×4 diagonal matrix of proportional gains and K_d is a 4×4 diagonal matrix of derivative gains. In the simulation model, h in (S4) is quantized to the same level as the encoders on the robot, and \dot{h} is obtained by numerical differentiation. The control inputs are updated with a sampling time of 1 ms, which equals the sampling time used on the robot.

PHASE I, FLIGHT

The flight phase is characterized by the absence of contact with the ground. Because the robot is in the air and there is nothing to push against, the reference commands

$$h_I^{\text{ref}} = \begin{bmatrix} \pi - 0.5\delta_{LA} - h_T^d \\ \gamma_{LS \rightarrow mLS} h_{LS_L}^d \\ \pi + 0.5\delta_{LA} - h_T^d \\ \gamma_{LS \rightarrow mLS} h_{LS_R}^d \end{bmatrix} \quad (S5)$$

$$S_{I \rightarrow II} : \{p_{\text{toe}_L} = 0, p_{\text{toe}_R} = 0\}, \quad (S6)$$

focus on the robot's relative pose rather than the absolute orientation of a link with respect to a world frame. While the flight-phase controller runs until both legs are in contact with the ground, the time between one leg and the other impacting the ground is less than 20 ms, and hence for most of this phase the robot is in the air.

Constant setpoints are chosen for the controlled variables (S3). Specifically, the commands $q_{LA_L} = \pi - 0.5\delta_{LA} - h_T^d$ and $q_{LA_R} = \pi + 0.5\delta_{LA} - h_T^d$ regulate the relative angle between the legs to a desired value of δ_{LA} and orient the legs with respect to a nominal torso angle of h_T^d . The commands

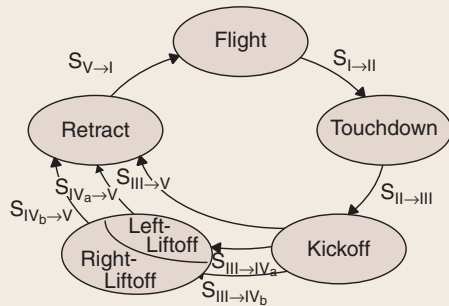


FIGURE S3 Hopping controller phases and transitions. From phase III, three possible transitions can occur because which leg first comes off the ground cannot be predicted. According to which leg comes off the ground, the controller selects phase IV_a , IV_b , or V as the next phase.

$q_{mLS_L} = \gamma_{LS \rightarrow mLS} h_{LS_L}^d$ and $q_{mLS_R} = \gamma_{LS \rightarrow mLS} h_{LS_R}^d$ regulate the lengths of the left and right legs to nominal values $h_{LS_L}^d$ and $h_{LS_R}^d$, respectively; equivalently, these commands can be thought of as setting the knee angles at appropriate values for absorbing the subsequent impact. The gear ratios $\gamma_{LS \rightarrow mLS}$ and $\gamma_{LS \rightarrow mLS}$ are present because the controlled variables are motor positions.

PHASE II, TOUCHDOWN

With both legs firmly on the ground, the reference command becomes

$$h_{II}^{\text{ref}} = \begin{bmatrix} q_T + q_{LA_R} - h_T^d - \delta_{LA} \\ \gamma_{LS \rightarrow mLS} h_{LS_L}^d \\ q_T + q_{LA_R} - h_T^d \\ \gamma_{LS \rightarrow mLS} h_{LS_R}^d \end{bmatrix}, \quad (S7)$$

$$S_{II \rightarrow III} : \{|\dot{p}_{\text{hip}}^v| < 0.0225\}. \quad (S8)$$

The leg-angle motors are now used to regulate the absolute orientation of the torso to h_T^d and the relative angle between the legs to δ_{LA} . The leg-shape motor positions q_{mLS_L} and q_{mLS_R} continue to be commanded to constant values so that the springs absorb the impact energy. The transition to the kickoff phase occurs when the vertical velocity of the center of mass approaches zero.

PHASE III, KICKOFF

When the vertical component of the center of mass velocity approaches zero, the reference command is changed to

Even though sustained hopping is not achieved, the data from the experiments can be used to identify the parameters in the hard-stop, cable stretch, and compliant-ground-contact models. The parameter fitting is accomplished with a combination of hand adjust-

ment and nonlinear least squares. The resulting parameters are given in Table 8. Plots demonstrating the closeness of fit of the model to the identification data are not shown for reasons of space. Instead, validation data is reported.

$$h_{III}^{\text{ref}} = \begin{bmatrix} q_T + q_{LA_R} - h_T^d - \delta_{LA} \\ \gamma_{LS \rightarrow mLS} h_{LS_L}^d - \gamma_{LS \rightarrow mLS} \delta_{LS_L}^- \\ q_T + q_{LA_R} - h_T^d \\ \gamma_{LS \rightarrow mLS} h_{LS_R}^d - \gamma_{LS \rightarrow mLS} \delta_{LS_R}^- \end{bmatrix}, \quad (\text{S9})$$

$$S_{III \rightarrow IV_a} : \{p_{\text{toe}_L} > 0, p_{\text{toe}_R} \leq 0\}, \quad (\text{S10})$$

$$S_{III \rightarrow IV_b} : \{p_{\text{toe}_L} \leq 0, p_{\text{toe}_R} > 0\}, \quad (\text{S11})$$

$$S_{III \rightarrow V} : \{p_{\text{toe}_L} > 0, p_{\text{toe}_R} > 0\}. \quad (\text{S12})$$

To propel the robot off the ground, the legs are extended by $\delta_{LS_L}^-$ for the left leg and $\delta_{LS_R}^-$ for the right leg. The remaining commands are unchanged. From phase III, three possible transitions can occur because which leg comes off the ground first cannot be predicted, and, with a 1-ms update rate, it is possible that both legs are observed to leave the ground simultaneously. According to leg liftoff order, the controller chooses phase IV_a, IV_b, or V as the next phase.

PHASE IV_A, LEFT-LIFTOFF

When the left leg lifts off the ground while the right leg remains in contact with the ground, the reference command becomes

$$h_{IV_a}^{\text{ref}} = \begin{bmatrix} H_1 h_{III}^{\text{ref}}(t_{III}^*) \\ \gamma_{LS \rightarrow mLS} h_{LS_L}^d + \gamma_{LS \rightarrow mLS} \delta_{LS_L}^+ \\ H_3 h_{III}^{\text{ref}}(t_{III}^*) \\ \gamma_{LS \rightarrow mLS} h_{LS_R}^d - \gamma_{LS \rightarrow mLS} \delta_{LS_R}^- \end{bmatrix}, \quad (\text{S13})$$

$$S_{IV_a \rightarrow V} : \{p_{\text{toe}_R} > 0\}, \quad (\text{S14})$$

where $H_1 = [1 \ 0 \ 0 \ 0]$, $H_3 = [0 \ 0 \ 1 \ 0]$, and t_{III}^* is the time when the transition from phase III occurs. The left leg starts to retract by $\delta_{LS_L}^+$ to provide clearance. The leg-angle positions are held at their values the end of phase III.

PHASE IV_B, RIGHT-LIFTOFF

When the right leg lifts off the ground while the left leg remains in contact with the ground, the reference command becomes

$$h_{IV_b}^{\text{ref}} = \begin{bmatrix} H_1 h_{III}^{\text{ref}}(t_{III}^*) \\ \gamma_{LS \rightarrow mLS} h_{LS_L}^d - \gamma_{LS \rightarrow mLS} \delta_{LS_L}^- \\ H_3 h_{III}^{\text{ref}}(t_{III}^*) \\ \gamma_{LS \rightarrow mLS} h_{LS_R}^d + \gamma_{LS \rightarrow mLS} \delta_{LS_R}^+ \end{bmatrix}, \quad (\text{S15})$$

$$S_{IV_b \rightarrow V} : \{p_{\text{toe}_L} > 0\}. \quad (\text{S16})$$

The notation is as in phase IV_a. The right leg starts to retract by $\delta_{LS_R}^+$ to provide clearance. The leg-angle positions are held at their values the end of phase III.

PHASE V, RETRACT

Once both legs lift off the ground, the retraction phase is held for 50 ms, after which the controller passes to the flight phase. The reference command is

$$h_V^{\text{ref}} = \begin{bmatrix} H_1 h_{III}^{\text{ref}}(t_{III}^*) \\ \gamma_{LS \rightarrow mLS} h_{LS_L}^d + \gamma_{LS \rightarrow mLS} \delta_{LS_L}^+ \\ H_3 h_{III}^{\text{ref}}(t_{III}^*) \\ \gamma_{LS \rightarrow mLS} h_{LS_R}^d + \gamma_{LS \rightarrow mLS} \delta_{LS_R}^+ \end{bmatrix}, \quad (\text{S17})$$

$$S_{V \rightarrow I} : \{t = t_v^* + 0.05\}, \quad (\text{S18})$$

where t_v^* is the time when the transition to phase V occurs. Otherwise, the notation is as in phase IV_a. The leg-angle positions are held at their values the end of phase III. Both legs are retracted to provide clearance.

PARAMETER VALUES

Applying the above controller to the identified model, a periodic solution is found with the controller parameter values

$$\begin{aligned} \delta_{LA} &= 0.524 \text{ rad } (30^\circ), & h_T^d &= 0.140 \text{ rad } (8^\circ), \\ h_{LS_L}^d &= 0.209 \text{ rad } (12^\circ), & h_{LS_R}^d &= 0.209 \text{ rad } (12^\circ), \\ \delta_{LS_L}^- &= 0.087 \text{ rad } (5^\circ), & \delta_{LS_R}^- &= 0.227 \text{ rad } (13^\circ), \\ \delta_{LS_L}^+ &= 0.087 \text{ rad } (5^\circ), & \delta_{LS_R}^+ &= 0.087 \text{ rad } (5^\circ), \end{aligned}$$

with the robot's horizontal position over one hop translated backward by 0.27 m, which corresponds to $\delta\phi_h^d = -0.273 \text{ rad} = -6.9^\circ$ of rotation as measured by the encoder on the central tower.

Simulation shows that the periodic motion is unstable. The orbit is stabilized with an event-based controller that updates the commanded torso angle h_T^d based on the distance traveled horizontally during one hop, namely,

$$\begin{aligned} \phi_h[k] &= \phi_h(t_{I \rightarrow II}), \\ \delta h_T^d[k] &= K_T(\phi_h[k] - \phi_h[k-1] - \delta\phi_h^d), \\ h_T^d[k] &= h_T^{d0} + \delta h_T^d[k], \end{aligned}$$

where k is the hopping count, $t_{I \rightarrow II}$ is the time when the transition from phase I to phase II occurs, and K_T is a gain. If MABEL travels less than $\delta\phi_h^d$ during the previous hop, the torso is leaned backward from the nominal value h_T^{d0} , and vice versa if the robot travels more than $\delta\phi_h^d$.

A few hours of parameter tuning with the simulation model resulted in a stabilizing controller, while days of trial and error in the laboratory were unsuccessful.

Hopping Experiments for Validation

When the nominal hopping controller is simulated on the identified model, the closed-loop system is found to be unstable. Event-based updates to the torso angle are therefore added to achieve stability, as explained in "How

Hopping Is Achieved." The controller is then applied to MABEL, resulting in 92 hops before the test is deliberately terminated. The data are presented next.

Figures 19–22 compare typical experimental results against the simulation results for the 31st and 32nd hops.

TABLE 8 Parameters estimated from the dynamic hopping experiment.

Spring Model

Kd_B (N-m-s/rad)	1.5	K_{vd1} (N-m-s/rad)	1000
K_{d1} (N-m-s/rad)	100	K_{vd2} (N-m/(rad/s) ^{0.5})	50

Cable Stretch Model

	$i = mLS_L$	$i = mL_A_L$	$i = mLS_R$	$i = mL_A_R$
$K_{C,i}$ (N-m/rad)	2.9565	3.5000	2.9565	3.8094
$Kd_{C,i}$ (N-m-s/rad)	0.0402	0.0889	0.0804	0.3556
Ground Model				
λ_v^a (N/m ^{1.5} /(m/s))	3.0e6	σ_{h0} (N/m)	260.0	
λ_v^b (N/m ^{1.5} /(m/s) ^{0.5})	4.5e6	σ_{h1} (N-s/m)	2.25	
n	1.5	α_{h0} (N)	1.71	
K (N/m ^{1.5})	4.38e7	α_{h2} (N-s/m)	0.54	

Figures 19 and 20 depict joint position angles. It is observed that the period of the experimental data is longer than that of the simulation results by approximately 30 ms. Because the hopping controller regulates four outputs computed from q_T , q_{LA_L} , q_{LA_R} , q_{mLS_L} , and q_{mLS_R} , it could be argued that the closeness of the simulated and experimental values is a reflection of the controller. However, the spring compressions q_{BSP_L} and q_{BSP_R} , as well as the horizontal and vertical hip positions p_{hip}^h and p_{hip}^v , are unregulated, and Figure 20 shows that these variables are captured by the model.

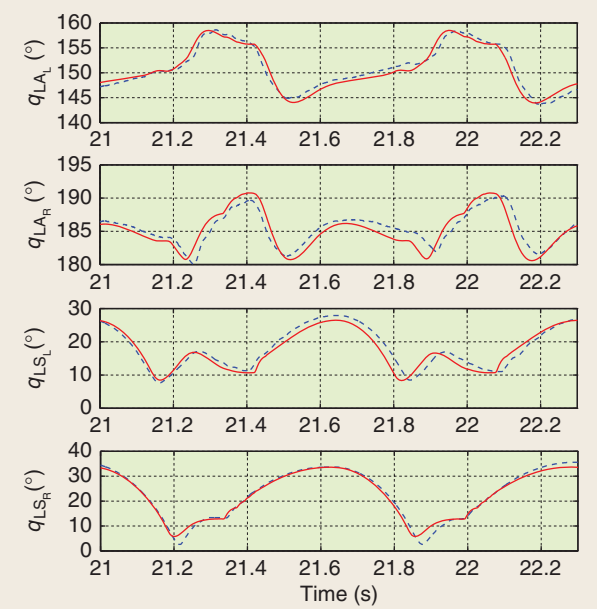


FIGURE 19 Validation data from the second hopping experiment. The joint positions for the simulation are indicated by solid red lines, while the joint positions for the experiment are indicated by dotted blue lines. Though the hopping controller is not based on trajectory tracking, the variables shown are indirectly regulated by the feedback controller, which may be responsible for the close correspondence between the modeled and measured data.

Figure 21 depicts joint torques. The simulation predicts the joint torques observed in the experiment with an RMS error of 1.0 N-m. The ability to predict torque is an accepted measure of fit for models of mechanical systems [11], [33]–[36].

Figure 22 compares the measured and simulated cable stretch, in degrees of motor rotation. Up to 200° of cable stretch is observed. The maximum error in the modeled response occurs in the right leg angle. The predicted ground reaction forces are not compared to experimental data because MABEL is not equipped with force sensors.

MODEL-BASED CONTROL OF WALKING ON UNEVEN GROUND

The boom and central tower arrangement constrain MABEL to the laboratory. Nevertheless, the robot can be used to investigate locomotion over uneven ground by varying the height of the floor on which it is walking. The robotics literature considers a step-down test as a measure of gait stability [37]–[39]. In this test, the robot walks on a flat section of floor, followed by a step down to another flat section of floor, as

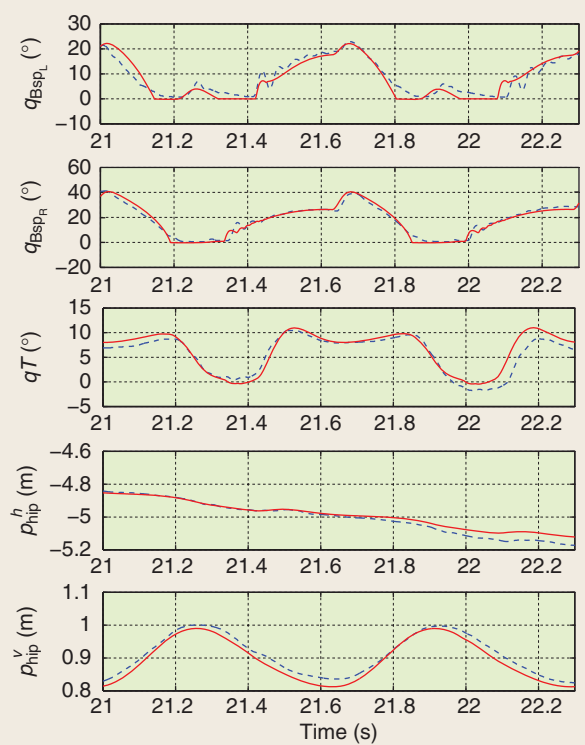


FIGURE 20 Validation data from the second hopping experiment. The joint and hip positions for the simulation are indicated by solid red lines, while the joint and hip positions for the experiment are indicated by dotted blue lines. For these variables, the close correspondence between the modeled and the measured data supports the model.

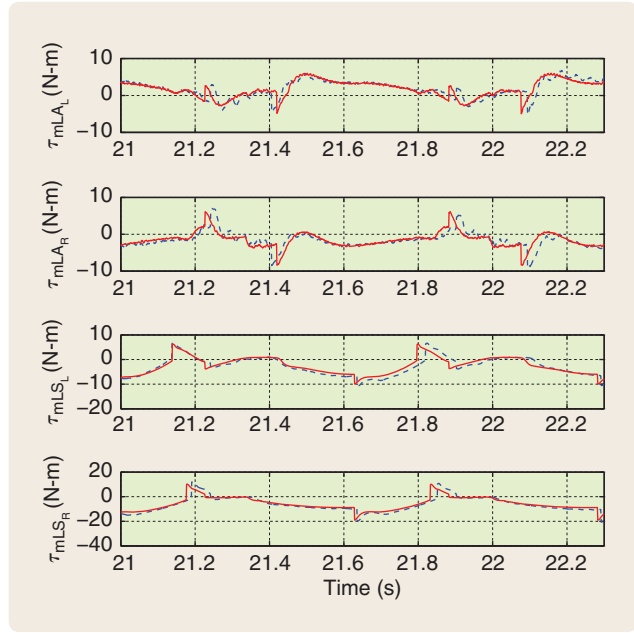


FIGURE 21 Validation data from the second hopping experiment. The motor torques for the simulation are indicated by solid red lines, while the motor torques for the experiment are indicated by dotted blue lines. The ability to predict torque is an accepted measure of fit for models of mechanical systems.

illustrated in Figure 23. The farther a robot can step down without falling, the better. A key point here is that the robot is provided information on neither where the step down occurs, nor by how much.

FEEDBACK LAW DESIGN

How far can MABEL step down without falling? The question as given is incorrectly posed, because MABEL cannot walk without a feedback law. The robustness of a walking gait is a property of the closed-loop system consisting of the robot and the controller. We use the method of virtual constraints to design feedback laws [40]. The essential idea of this method is to design outputs for the robot's model in the form

$$y = h(q), \quad (33)$$

which depend only on the configuration variables. If a feedback can be found such that the output y is driven asymptotically to zero, then the solutions of the closed-loop system asymptotically satisfy $h(q) = 0$, which has the form of a holonomic constraint on a mechanical system.

Holonomic constraints in mechanical systems are typically realized by interconnections of gears and linkages; moreover, the constraints are “workless” in that D'Alembert's principle implies that the Lagrange multipliers associated with the constraints, that is, the generalized forces and torques that impose the constraints,

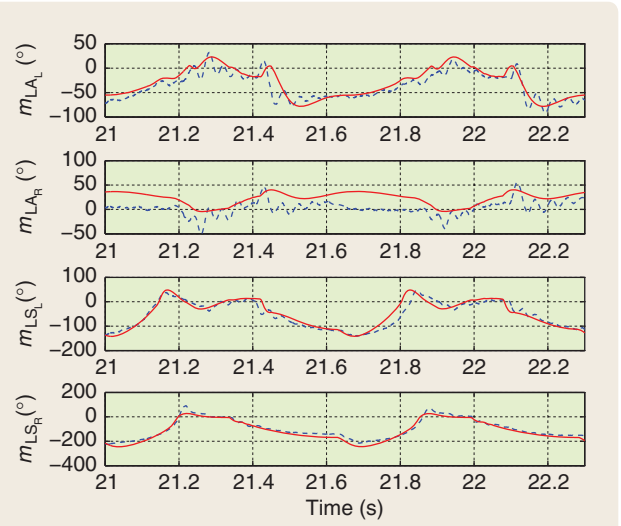


FIGURE 22 Validation data from the second hopping experiment. Cable stretch for the simulation is indicated by solid red lines, while cable stretch for the experiment is indicated by dotted blue lines. When the gear ratios are taken into account, 100° of cable stretch results in 4.25° of displacement in q_{LA} and 3.18° of displacement in q_{LS} .

do no work on the system. For MABEL, the actuators do perform work on the system when zeroing the output, and the constraints are realized only asymptotically. To modify a physical constraint, the gears or linkages must be changed, whereas the constraints (33) can be changed on the fly by modifying a few lines of code in the embedded controller. For these reasons, the outputs (33) are referred to as virtual constraints [41].

We use virtual constraints to synchronize the evolution of MABEL's links throughout a stride to synthesize a walking gait. One virtual constraint per actuator is specified in the form “output equals controlled variables minus desired evolution.” Specifically,

$$y = h_0(q) - h^d(s, \alpha), \quad (34)$$

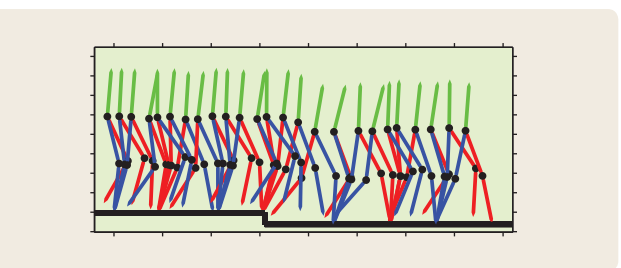


FIGURE 23 Stick figure illustration of a step-down experiment. The robot walks on a flat section of flooring and then steps down to another flat section of flooring. The robot blindly walks off the raised section of flooring; no information on where the step-down occurs, or the magnitude of the step is provided to the robot. This figure is generated from experimental data of MABEL stepping down from a height of 3.5 in (8.89 cm).

Using the identified model, a new set of virtual constraints is computed that reduces the impact intensity of the second step by approximately 40%.

where the controlled variables are

$$h_0(q) = \begin{bmatrix} q_{\text{mLS}_{\text{st}}} \\ q_{\text{LA}_{\text{sw}}} \\ q_{\text{mLS}_{\text{sw}}} \\ q_{\text{T}} \end{bmatrix}, \quad (35)$$

and where $q_{\text{mLS}_{\text{st}}}$ is the leg-shape-motor position of the stance leg, $q_{\text{LA}_{\text{sw}}}$ and $q_{\text{mLS}_{\text{sw}}}$ are the leg angle and leg-shape-motor position of the swing leg, and q_{T} is the torso angle. The desired evolution of the controlled variables in (35) is specified by the functions $h_{\text{mLS}_{\text{st}}}^d$, $h_{\text{LA}_{\text{sw}}}^d$, $h_{\text{mLS}_{\text{sw}}}^d$, and h_{T}^d , respectively, and assembled as

$$h^d(s, \alpha) = \begin{bmatrix} h_{\text{mLS}_{\text{st}}}^d(s, \alpha) \\ h_{\text{LA}_{\text{sw}}}^d(s, \alpha) \\ h_{\text{mLS}_{\text{sw}}}^d(s, \alpha) \\ h_{\text{T}}^d(s, \alpha) \end{bmatrix}, \quad (36)$$

where α is a vector of real numbers parameterizing the virtual constraints. For MABEL, we choose s as

$$s(q) = \frac{\theta(q) - \theta^+}{\theta^- - \theta^+}, \quad (37)$$

where θ is the absolute angle formed by the virtual compliant leg relative to the ground, that is,

$$\theta(q) = \pi - q_{\text{LA}_{\text{st}}} - q_{\text{T}}, \quad (38)$$

and θ^+ and θ^- are the values of $\theta(q)$ at the beginning and end of a step, respectively. How to construct the functions in $h^d(s, \alpha)$ from Bézier polynomials and how to choose the parameters to create a periodic walking gait in the closed-loop system is explained in [40] and [9]. The key idea is to select α to minimize a cost function representing energy supplied by the actuators, normalized by step length, with the minimization subject to boundary conditions that specify a periodic solution, actuator magnitude and power limitations, friction limits in the ground contact model, swing-leg clearance, and desired walking speed.

In principle, the virtual constraints can be implemented on the robot by any feedback capable of driving y to zero. In the experiments described below, we use the feedforward-plus-PD-controller

$$u_{\text{exp}}(q, \dot{q}) = u^*(s(q), \alpha) - K_p y - K_D \dot{y}, \quad (39)$$

where $u^*(s(q), \alpha)$ is nominal torque along the periodic orbit determined from the parameter optimization problem

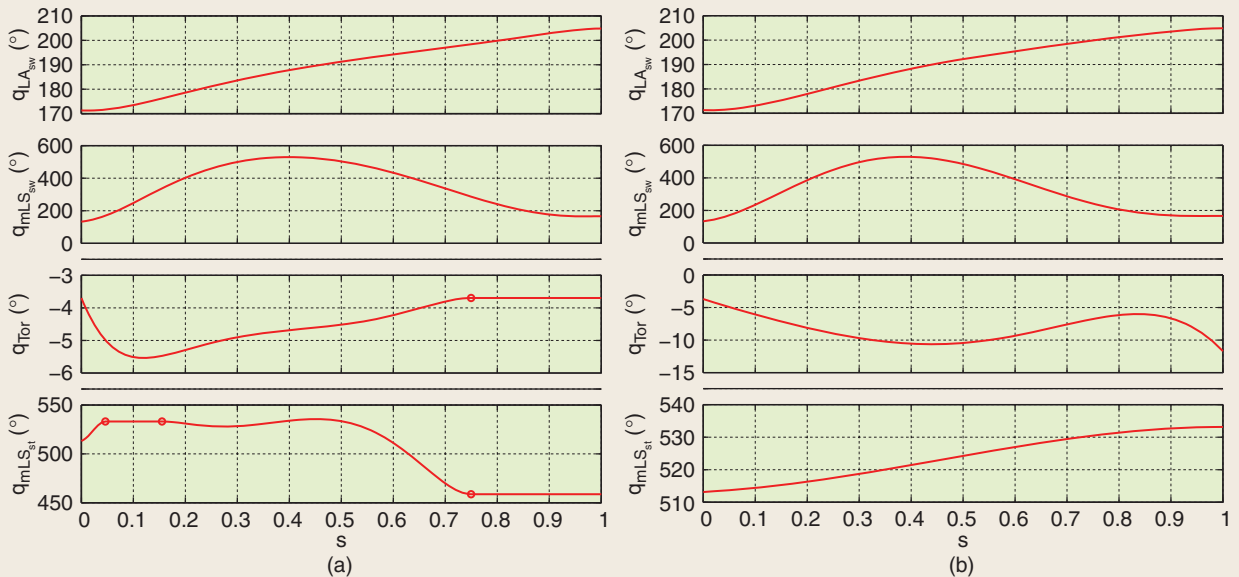


FIGURE 24 Virtual constraints used in the feedback controller. (a) shows the constraints used in the first step-down experiment. (b) shows the additional virtual constraints used in the switching controller of the second step-down experiment.

A hopping gait is used to complete the identification of, and subsequently validate, the overall dynamic model of MABEL.

when designing the gait, and γ is defined in (34). The asymptotic stability of the periodic orbit under this feedback law is verified on the model with a Poincaré map, as explained in [40] and [9].

The above process results in the virtual constraints depicted in Figure 24(a). These constraints correspond to a nominal walking gait from [9], which is modified so that the end of the swing leg can clear a 2-cm obstacle, allowing the robot to step onto a platform before stepping off it. In addition, the torso angle is adjusted so that the average walking speed is 0.95 m/s.

First Step-Down Test

For the step-down test, MABEL is put in motion, walking around the central tower on an initially flat floor. At the end of each lap, MABEL walks up a stair-stepped ramp, takes at least one step on a flat platform, and then steps off the platform. The height of the platform is increased each lap until the robot falls. Figure 25 illustrates how the ramp and platform are constructed from a combination of 0.5 in and 1.0 in (2.54 cm) thick sheets of plywood.

Using the control law (39) and the virtual constraints of Figure 24(a), MABEL succeeds in stepping off heights of 0.5, 1.0, 1.5, and 2.0 in, before falling when the platform height is increased to 2.5 in (6.35 cm). A video of the experiment is available at [42].

The fall is rather spectacular. MABEL steps off the platform onto its left leg, with no apparent difficulty, but on the next step, when the right leg impacts the ground, the shin separates into two pieces, causing the fall. In the video, the shin appears to suffer a devastating break, but in reality, it is quite benign. To protect the ball bearings in the knees and hips from damage during experiments such as this one, the shin contains a “mechanical fuse,” as shown in Figure 26. The mechanical fuse joins the two pieces of the shin by plastic pins, which give way under a sufficiently high impact. It takes about an hour to reassemble the shin.

Because the robot is not equipped with force sensors, it is not immediately obvious whether the mechanical fuse is activated because the plastic pins are worn or because the impact forces are exceptionally large. Using the impact model of [43], however, which is based on the change in generalized momentum when two objects collide, the contact intensity I_F at the leg end can be estimated from the experimental data. I_F has units of N-s and represents, roughly speaking, the integral of the contact force over the duration of the contact event. Table 9 and Figure 27 show

the estimated contact intensity when walking on flat ground and when stepping off several raised platforms. The data indicate that, upon stepping off the 2.5 in platform, the contact event of the second step is more than four times as intense as when walking on flat ground.

The step off the platform is expected to result in a more intense impact than the second step. Further analysis of the data reveals what is happening. Figure 28 shows how the disturbance at step-down causes the torso to pitch forward. The feedback system overreacts when correcting the torso angle,



FIGURE 25 Plywood boards used to form a stair-stepped platform. By combining boards that are 1 in (2.54 cm) and 0.5 in (1.27 cm) thick, platforms of a desired height are assembled.

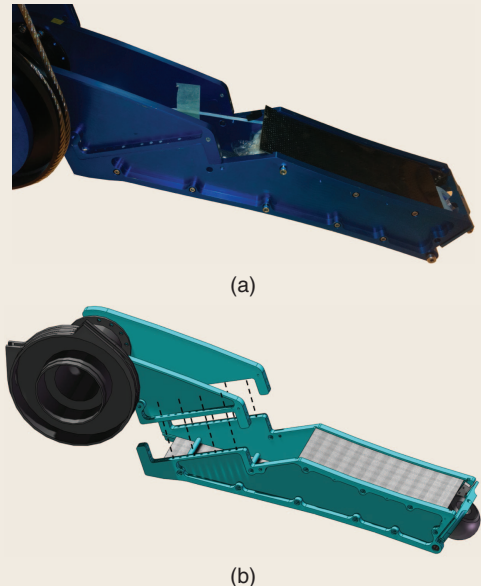


FIGURE 26 Mechanical fuse in the shin. The shin of the robot is in (a), while (b) provides an exploded view from the CAD drawings. The two parts of the shin are affixed with plastic pins. The pins shear if the leg-ground impact generates a sufficiently large force, thus protecting other parts of the robot, such as the knee and hip ball bearings, from damage.

TABLE 9 Estimated contact impulse I_F on the swing leg for the initial step-down experiment. The horizontal and vertical components I_F^h and I_F^v are given for the first and second steps, where the first step is the step off the platform. The data show that the leg experiences larger forces on the second step. This behavior points to a problem with the controller's response to the step-down disturbance. The leg breaks on the second step off the 2.5-in (6.35-cm) platform, when the contact impulse is estimated to exceed four times its mean value for walking on flat ground.

	Flat Ground		1.0 in		1.5 in		2.0 in		2.5 in		Height Step
	Mean		First	Second	First	Second	First	Second	First	Second	
I_F^h	-3.3		-2.5	-2.9	-2.7	-5.2	-2.9	-5.3	-4.0	-11.1	N-s
I_F^v	13.3		15.4	14.3	16.5	20.6	15.3	24.4	22.2	46.5	N-s

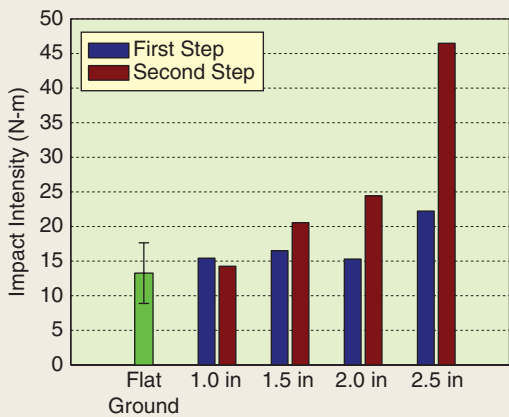


FIGURE 27 Impact intensity calculated from the first step-down experiment. Only the vertical component is displayed. The green bar shows the average impact intensity when walking on flat ground; the bars show \pm one standard deviation. The blue bar shows the impact intensity upon step-down, while the red bar shows impact intensity for the ensuing step. The larger impact intensity on the step following the 2.5 in (6.35 cm) step-down leads to the fuse activating in the shin.

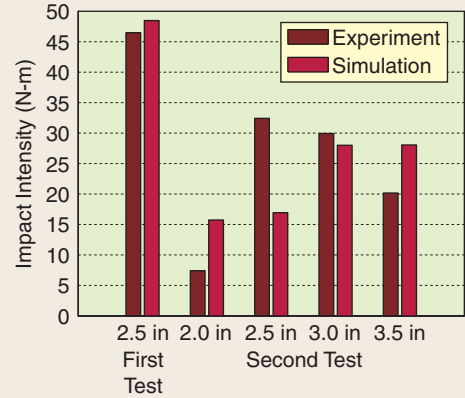


FIGURE 29 Impact intensities of the second step-down experiment. The brown bar is the vertical component of the impact intensity of the second step, computed from the experimental data. The bright red bar shows the values predicted by the simulation.

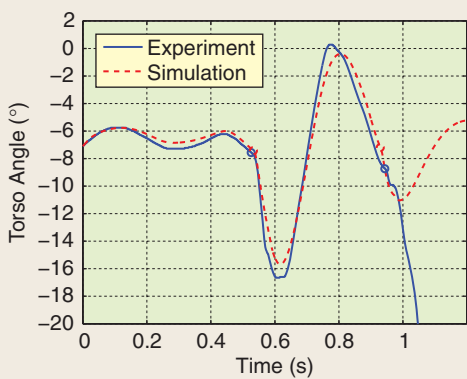


FIGURE 28 Experimental and simulation data of the torso angle when stepping down from the 2.5-in platform. The forward direction is counterclockwise and hence corresponds to decreasing angles. The red and blue circles show when the swing leg impacts the ground. The torso undergoes a large oscillation as a result of the disturbance at step-down. The same behavior is observed in the model and the experiment with the exception that, on the second step at 0.943 s, the robot's leg breaks, causing the torso to continue rotating forward.

causing a second, rapid, forward-pitching motion of the torso. Because the angle of the swing leg is controlled relative to the torso, the swing leg rotates forward rapidly as well and impacts the ground with sufficient force to activate the fuse in the shin. Simulation of the model developed in this article confirms this sequence of events, with the exception that the model cannot predict that the shin actually breaks.

Second Step-Down Test

When MABEL steps off a platform, the height of the platform can be immediately computed at impact from the lengths of the legs and the angles of the joints. This information can be used in the ensuing step to attenuate disturbances. Using the identified model, a new set of virtual constraints is computed that reduces the impact intensity of the second step by approximately 40%. These constraints are depicted in Figure 24(b).

The controller is modified to include a switch, as in [44]. The original virtual constraints of Figure 24(a) are used in (34) and (39) until a step-down exceeding 2 cm is detected. The detection of the step-down height takes place when the leg contacts the ground. For the ensuing step, the virtual constraints of Figure 24(b) are substituted into (34), whereas, on the next step, the original virtual constraints are reapplied.

Using the identified model, a new set of virtual constraints is computed that reduces the impact intensity of the second step by approximately 40%.

With this modification to the control law, the step-down experiment is repeated. MABEL steps down without falling from heights of 2.5, 3.0, and 3.5 in (8.89 cm), at which point the experiment is terminated, without the robot falling. Figure 29 shows the estimated impact intensities for these tests.

CONCLUSIONS

Parameter identification of MABEL, a five-link bipedal robot with a compliant transmission, has been studied. For each side of the robot, the transmission is composed of three cable differentials that connect two motors to the hip and knee joints in such a way that one motor controls the angle of the virtual leg consisting of the line connecting the hip to the toe, while the length of the virtual leg is controlled by a second motor connected in series with a spring. The springs serve both to isolate the rotor inertia of the leg-shape motors from the impact forces at leg touchdown and to subsequently store energy when the support leg must decelerate the downward motion of the robot's center of mass.

The robot is equipped with 15 encoders to measure motor, pulley, and joint angles, as well as contact switches at the ends of the legs to detect impact with the ground. Neither force sensors, torque sensors, nor accelerometers are available. To circumvent these limitations, the identification procedure took advantage of the modular nature of the robot. By selectively disconnecting cables in the transmission, various elements can be isolated for individual study, simplifying the parameter identification process.

MABEL has two kinds of compliance. One is the unilateral, fiberglass springs designed into the transmission. The other source of compliance is unplanned and arises from the stretching of the cables between the pulleys. The compliance of the unilateral spring was obtained by means of static loading experiments. The compliance from cable stretch was estimated from short-duration hopping experiments. From the same data set, the parameters for a compliant ground model were also roughly estimated. The experiments lasted only a few hops because we were unable to stabilize the hopping gait without a model; trial and error in the laboratory did not work.

The utility of the model was illustrated by using it to redesign the hopping controller. When the redesigned controller was implemented on the robot, 92 hops were made, at which point the experiment was terminated. The utility of the model was further illustrated in a set of step-down experiments. On the basis of the model, we were able to increase the robustness of a walking gait so that the robot

could step down, blindly, from a platform raised 3.5 in (8.89 cm) above the floor. The model is currently being used to maximize the energy efficiency of walking and to design controllers for running gaits.

ACKNOWLEDGMENTS

This work is supported by NSF grant ECS-909300. The authors thank J. Koncsol for his selfless dedication to our project. His time in the laboratory, on his way to work, or on Saturday mornings, where he shared his extensive experience in electronic circuit design and testing, was instrumental to our experiments. G. Buche is gratefully acknowledged for his many contributions, especially the design of the power supply and safety systems. His prior experience with Rabbit was invaluable in the initial setup of the MABEL testbed.

AUTHOR INFORMATION

Hae-Won Park (parkhw@umich.edu) is a Ph.D. candidate in the Department of Mechanical Engineering, University of Michigan, Ann Arbor. He received the B.S. and M.S. in mechanical engineering from Yonsei University, Seoul, South Korea, in 2005 and 2007, respectively. He started his doctorate at the University of Michigan in 2007. His research interests are in modeling, system identification, and control of robotic systems. He can be contacted at 1303 Beal Ave., 4303 EECS Building, University of Michigan, Ann Arbor, Michigan 48109-2111, USA.

Koushil Sreenath is a Ph.D. candidate in the Electrical Engineering and Computer Science Department at the University of Michigan, Ann Arbor. He received the B.E. from PES Institute of Technology, Bangalore, India, in 2002 and the M.S. from the University of Texas, Arlington, in 2005. From 2006 to 2007, he was a research engineer with the Intelligent Controls Group, Saint-Gobain R&D, Northboro, Massachusetts. His research interests are in modeling, feedback design, and experiments in legged robotics, as well as adaptive sampling and resource allocation in mobile wireless sensor networks.

Jonathan W. Hurst is an assistant professor of mechanical engineering at Oregon State University. He received the B.S. in mechanical engineering, the M.S. in robotics, and the Ph.D. in robotics from Carnegie Mellon University, Pittsburgh, Pennsylvania, in 2001, 2004, and 2008, respectively. He designed and built MABEL while a Ph.D. student. His research interests include legged locomotion, natural dynamics, and robot actuation, with special interest in the role and implementation of compliance in legged locomotion.

Jessy W. Grizzle is a professor of electrical engineering and computer science at the University of Michigan, Ann Arbor, where he also holds the Jerry and Carol Levin professorship. He is a Fellow of the IEEE. He jointly holds 16 patents dealing with emissions reduction in passenger vehicles through improved control system design. His work on bipedal locomotion has been presented in numerous plenary lectures and has been featured in *The Economist*, *Wired Magazine*, *Discover Magazine*, *Scientific American*, and several television programs.

REFERENCES

- [1] S. Collins, A. Ruina, R. Tedrake, and M. Wisse, "Efficient bipedal robots based on passive-dynamic walkers," *Science*, vol. 307, pp. 1082–1085, 2005.
- [2] J. K. Hodgins, "Biped gait transitions," in *Proc. IEEE Int. Conf. Robotics and Automation*, Sacramento, CA, Apr. 1991, pp. 2092–2097.
- [3] J. K. Hodgins and M. H. Raibert, "Adjusting step length for rough terrain locomotion," *IEEE Trans. Robot. Automat.*, vol. 7, no. 3, pp. 289–298, June 1991.
- [4] M. H. Raibert, *Legged Robots That Balance*. Cambridge, MA: MIT Press, 1986.
- [5] C. Chevallereau, G. Abba, Y. Aoustin, F. Plestan, E. Westervelt, C. Canudas-De-Wit, and J. Grizzle, "RABBIT: A testbed for advanced control theory," *IEEE Control Syst. Mag.*, vol. 23, no. 5, pp. 57–79, Oct. 2003.
- [6] E. R. Westervelt, G. Buche, and J. W. Grizzle, "Experimental validation of a framework for the design of controllers that induce stable walking in planar bipeds," *Int. J. Robot. Res.*, vol. 24, no. 6, pp. 559–582, June 2004.
- [7] B. Morris, E. Westervelt, C. Chevallereau, G. Buche, and J. Grizzle, "Achieving bipedal running with RABBIT: Six steps toward infinity," in *Proc. Fast Motions Symp. Biomechanics and Robotics*, K. Mombaur and M. Dheil, Eds. Heidelberg, Germany: Springer-Verlag, 2006, pp. 277–297.
- [8] J. W. Hurst, J. E. Chestnutt, and A. A. Rizzi, "The actuator with mechanically adjustable series compliance," *IEEE Trans. Robot.*, vol. 26, no. 4, pp. 597–606, 2010.
- [9] K. Sreenath, H.-W. Park, I. Poulikakos, and J. W. Grizzle, "A compliant hybrid zero dynamics controller for stable, efficient and fast bipedal walking on MABEL," *Int. J. Robot. Res.*, Sept. 21, 2010. [Online]. Available: <http://ijr.sagepub.com/content/early/2010/09/16/0278364910379882.abstract>
- [10] W. Khalil and E. Dombre, *Modeling, Identification and Control of Robots*. Bristol, PA: Taylor & Francis, 2002.
- [11] J. Swevers, W. Verdonck, and J. D. Schutter, "Dynamic model identification for industrial robots," *IEEE Control Syst. Mag.*, vol. 27, no. 5, pp. 58–71, Oct. 2007.
- [12] C. G. Atkeson, C. H. An, and J. M. Hollerbach, "Estimation of inertial parameters of manipulator loads and links," *Int. J. Robot. Res.*, vol. 5, no. 3, pp. 101–119, 1986.
- [13] M. Gautier and W. Khalil, "On the identification of the inertial parameters of robots," in *Proc. IEEE Conf. Decision and Control*, Tampa, FL, Dec. 1988, pp. 2264–2269.
- [14] J. Hurst, J. Chestnutt, and A. Rizzi, "Design and philosophy of the Bi-MASC, a highly dynamic biped," in *Proc. IEEE Int. Conf. Robotics and Automation*, Roma, Italy, Apr. 2007, pp. 1863–1868.
- [15] J. Grizzle, J. Hurst, B. Morris, H.-W. Park, and K. Sreenath, "MABEL, a new robotic bipedal walker and runner," in *Proc. American Control Conf.*, St. Louis, MO, June 2009, pp. 2030–2036.
- [16] J. W. Hurst. (2008, Aug.). The role and implementation of compliance in legged locomotion. Ph.D. dissertation, Robot. Inst., Carnegie Mellon Univ., Pittsburgh, PA [Online]. Available: http://www.ri.cmu.edu/publication/view.html?pub_id=6179
- [17] M. A. Daley and A. A. Biewener, "Running over rough terrain reveals limb control for intrinsic stability," *Proc. Nat. Acad. Sci.*, vol. 103, no. 42, pp. 15681–15686, 2006.
- [18] M. A. Daley, J. R. Usherwood, G. Felix, and A. A. Biewener, "Running over rough terrain: guinea fowl maintain dynamic stability despite a large unexpected change in substrate height," *J. Exp. Biol.*, vol. 209, no. 1, pp. 171–187, 2006.
- [19] J. Hodgins and M. Raibert, "Adjusting step length for rough terrain locomotion," *IEEE Trans. Robot. Automat.*, vol. 7, no. 3, pp. 289–298, June 1991.
- [20] K. Hashimoto, Y. Sugahara, H. Sunazuka, C. Tanaka, A. Ohta, M. Kawase, H. Lim, and A. Takanishi, "Biped landing pattern modification method with nonlinear compliance control," in *Proc. IEEE Int. Conf. Robotics and Automation*, Orlando, FL, May 2006, pp. 1213–1218.
- [21] M. Ogino, H. Toyama, and M. Asada, "Stabilizing biped walking on rough terrain based on the compliance control," in *Proc. IEEE/RSJ Int. Conf. Intelligent Robots and Systems*, San Diego, CA, Nov. 2007, pp. 4047–4052.
- [22] U. Saranli, M. Buehler, and D. E. Koditschek, "RHEx: A simple and highly mobile hexapod robot," *Int. J. Robot. Res.*, vol. 20, pp. 616–631, 2001.
- [23] T. Takuma, S. Hayashi, and K. Hosoda, "3D bipedal robot with tunable leg compliance mechanism for multi-modal locomotion," in *Proc. IEEE/RSJ Int. Conf. Intelligent Robots and Systems*, Nice, France, Sept. 2008, pp. 1097–1102.
- [24] A. Dabroom and H. Khalil, "Numerical differentiation using high-gain observers," in *Proc. IEEE Conf. Decision and Control*, San Diego, CA, 1997, pp. 4790–4795.
- [25] M. Mboup, C. Join, and M. Fleiss, "A revised look at numerical differentiation with an application to nonlinear feedback control," in *Proc. Mediterranean Conf. Control and Automation*, Ajaccio, France, 2008, pp. 1–6.
- [26] J. Swevers, W. Verdonck, and J. De Schutter, "Dynamic model identification for industrial robots," *IEEE Control Syst. Mag.*, vol. 27, no. 5, pp. 58–71, 2007.
- [27] S. Diop, J. W. Grizzle, P. E. Moraal, and A. Stefanopoulos, "Interpolation and numerical differentiation for observer design," in *Proc. American Control Conf.*, Baltimore, MD, 1994, pp. 1329–1333.
- [28] U. Saranli, M. Buehler, and D. E. Koditschek, "RHEx: A simple and highly mobile hexapod robot," *Int. J. Robot. Res.*, vol. 20, no. 1, pp. 616–631, July 2001.
- [29] J. Walter and M. Koch (2008) uBLAS—Basic Linear Algebra Subprograms Library [Online]. Available: <http://www.boost.org>
- [30] D. Marhefka and D. Orin, "Simulation of contact using a nonlinear damping model," in *Proc. IEEE Int. Conf. Robotics and Automation*, Minneapolis, MN, Apr. 1996, vol. 2, pp. 1662–1668.
- [31] C. Canudas de Wit, H. Olsson, K. Astrom, and P. Lischinsky, "A new model for control of systems with friction," *IEEE Trans. Automat. Control*, vol. 40, no. 3, pp. 419–425, Mar. 1995.
- [32] F. Plestan, J. Grizzle, E. Westervelt, and G. Abba, "Stable walking of a 7-DOF biped robot," *IEEE Trans. Robot. Automat.*, vol. 19, no. 4, pp. 653–668, Aug. 2003.
- [33] J. Swevers, C. Ganseman, D. Tukel, J. de Schutter, and H. Van Brussel, "Optimal robot excitation and identification," *IEEE Trans. Robot. Automat.*, vol. 13, no. 5, pp. 730–740, Oct. 1997.
- [34] F. Pfeiffer and J. Holzl, "Parameter identification for industrial robots," in *Proc. IEEE Int. Conf. Robotics and Automation*, Nagoya, Japan, May 1995, vol. 2, pp. 1468–1476.
- [35] P. Vandajan, M. Gautier, and P. Desbats, "Identification of robots inertial parameters by means of spectrum analysis," in *Proc. IEEE Int. Conf. Robotics and Automation*, Nagoya, Japan, May 1995, vol. 3, pp. 3033–3038.
- [36] K. Kozlowski, *Modelling and Identification in Robotics*. Secaucus, NJ: Springer-Verlag, 1998.
- [37] M. Wisse, A. L. Schwab, R. Q. van der Linde, and F. C. T. van der Helm, "How to keep from falling forward: Elementary swing leg action for passive dynamic walkers," *IEEE Trans. Robot.*, vol. 21, no. 3, pp. 393–401, June 2005.
- [38] C. Sabourin, O. Bruneau, and G. Buche, "Control strategy for the robust dynamic walk of a biped robot," *Int. J. Robot. Res.*, vol. 25, no. 9, pp. 843–860, Sept. 2006.
- [39] M. Wisse and R. Q. van der Linde, *Delft Pneumatic Biped*. New York: Springer-Verlag, 2007.
- [40] E. R. Westervelt, J. W. Grizzle, C. Chevallereau, J. H. Choi, and B. Morris, *Feedback Control of Dynamic Bipedal Robot Locomotion*. Boca Raton: CRC Press, 2007.
- [41] C. C. de Wit, "On the concept of virtual constraints as a tool for walking robot control and balancing," *Annu. Rev. Control*, vol. 28, no. 2, pp. 157–166, 2004.
- [42] J. W. Grizzle. (2009) Dynamic leg locomotion. YouTube Channel [Online]. Available: <http://www.youtube.com/DynamicLegLocomotion>
- [43] Y. Hurmuzlu and D. B. Marghitu, "Rigid body collisions of planar kinematic chains with multiple contact points," *Int. J. Robot. Res.*, vol. 13, no. 1, pp. 82–92, 1994.
- [44] T. Yang, E. Westervelt, and A. Serrani, "A framework for the control of stable aperiodic walking in underactuated planar bipeds," in *Proc. IEEE Int. Conf. Robotics and Automation*, Roma, Italy, Apr. 2007, pp. 4661–4666.

